

# SATURATED TORQUE FORMULA FOR PLANETARY MIGRATION IN VISCOUS DISKS WITH THERMAL DIFFUSION: RECIPE FOR PROTOPLANET POPULATION SYNTHESIS

F. S. MASSET<sup>1,2</sup>

Laboratoire AIM, CEA/DSM - CNRS - Université Paris Diderot, Irfu/Service d'Astrophysique, Bât. 709, CEA/Saclay, 91191 Gif-sur-Yvette, France

AND

J. CASOLI

Laboratoire AIM, CEA/DSM - CNRS - Université Paris Diderot, Irfu/Service d'Astrophysique, Bât. 709, CEA/Saclay, 91191 Gif-sur-Yvette, France

*Draft version October 30, 2018*

## ABSTRACT

We provide torque formulae for low mass planets undergoing type I migration in gaseous disks. These torque formulae put special emphasis on the horseshoe drag, which is prone to saturation: the asymptotic value reached by the horseshoe drag depends on a balance between coorbital dynamics (which tends to cancel out or saturate the torque) and diffusive processes (which tend to restore the unperturbed disk profiles, thereby desaturating the torque). We entertain here the question of this asymptotic value, and we derive torque formulae which give the total torque as a function of the disk's viscosity and thermal diffusivity. The horseshoe drag features two components: one which scales with the vortensity gradient, and one which scales with the entropy gradient, and which constitutes the most promising candidate for halting inward type I migration. Our analysis, which is complemented by numerical simulations, recovers characteristics already noted by numericists, namely that the viscous timescale across the horseshoe region must be shorter than the libration time in order to avoid saturation, and that, provided this condition is satisfied, the entropy related part of the horseshoe drag remains large if the thermal timescale is shorter than the libration time. Side results include a study of the Lindblad torque as a function of thermal diffusivity, and a contribution to the corotation torque arising from vortensity viscously created at the contact discontinuities that appear at the horseshoe separatrices. For the convenience of the reader mostly interested in the torque formulae, section 8 is self-contained.

*Subject headings:* Planetary systems: formation — planetary systems: protoplanetary disks — Accretion, accretion disks — Methods: numerical — Hydrodynamics

## 1. INTRODUCTION

Ever since the discovery of the first extrasolar planets, many efforts have been undertaken to account for the statistics of their orbital properties, and to link these statistics to the properties of the protoplanetary disk. In particular, the so-called planetary population synthesis models correspond to a class of essentially one dimensional models, in which the physics of the disk is treated so as to include, in a simplified manner, as many relevant physical processes as necessary, and in which the growth and migration of randomly sorted planetary embryos is tracked until the disk disappears (Thommes et al. 2008; Mordasini et al. 2009a; Ida & Lin 2008b,a, 2004b,a, 2005; Alibert et al. 2005; Thommes et al. 2007; Thommes & Murray 2006). The statistical properties inferred from these models can be confronted to observational data, and thus allow to constrain the underlying disk physical properties or the physics of the interaction of the embryos with the disk. One drawback of these models, however, is that they

have to rely on tidal torque expressions, since the processes that give rise to exchange of angular momentum between a planetary embryo and the disk cannot be captured by a one dimensional analysis.

A problematic phase arises in these models, that corresponds to the migration of low mass objects (the type I migration phase). Standard torque estimates, based on the linear expressions of Ward (1997) or Tanaka et al. (2002), yield a rapid flush of the low mass cores to the innermost parts of the protoplanetary disk. Several authors have circumvented this problem by arbitrarily lowering the type I migration estimate by an *ad hoc* factor  $f$  typically in the range  $f \sim 0.01 - 0.1$ , so as to allow a reasonable fraction of the initial cores to remain as sizable distances of the star over the disk lifetime (Ida & Lin 2008a; Mordasini et al. 2009b).

The theory of the tidal interaction of low mass planetary objects with the disk has recently changed, however, as Paardekooper & Papaloizou (2009a) have shown that one of the tidal torque components, the so-called corotation torque, eventually becomes non-linear at all planetary masses. This breakthrough renders obsolete the systematic use of the linear estimate of Tanaka et al. (2002) for low mass planets, and the torque expression that should be used is the sum of the linear Lindblad torque expression of Tanaka et al. (2002), and of the non-linear corotation torque. It corresponds to the torque

masset@fis.unam.mx  
jules.casoli@cea.fr

<sup>1</sup> On leave from Service d'Astrophysique, CE-Saclay, France. Now at Instituto de Ciencias Físicas, Universidad Nacional Autónoma de México (UNAM), Apdo. Postal 48-3, 62251-Cuernavaca, Morelos, México

<sup>2</sup> Send offprint requests to masset@fis.unam.mx

exerted by the coorbital region on to the planet. Only in the limit of low mass and large diffusion, does the corotation torque approaches its linear estimate. Far from this limit, the non-linear corotation amounts to the horseshoe drag, which corresponds to the torque exerted by fluid elements undergoing a horseshoe like libration in the coorbital region, in the frame corotating with the planet.

The horseshoe drag bears a number of similarities with the linear corotation torque: its scaling with all parameters (planet mass, disk surface density, disk aspect ratio, etc.) is the same, but it turns out to have in general a larger value. Another important difference is its long-term behavior: the horseshoe dynamics tends to redistribute angular momentum between the horseshoe region and the planet, but the total angular momentum content of the system composed of the planet and its coorbital region remains constant in an inviscid disk, if one disregards what is carried away by the wake. As a consequence, the horseshoe drag tends to zero on the long term, and the total angular momentum ever exchanged between the disk and a planet initially “switched on” in the unperturbed disk is simply the difference of angular momentum content of the horseshoe region between its final state and its initial, unperturbed state. This process, known as saturation, occurs on a relatively small time scale, typically of  $O(10^2)$  orbital periods for Earth-sized objects. It is in particular much shorter than the disk lifetime and the migration time scale itself, hence models that follow the migration of a core up to the disk dispersal should consider the long term value of the horseshoe drag (which we also call the asymptotic or saturated value), rather than the value that it displays soon after the introduction of the planet in an unperturbed disk (which we call the unsaturated value). As stressed above, if there is no process that allows the exchange of angular momentum between the horseshoe region and the rest of the disk, the asymptotic horseshoe drag is simply zero. If the disk has a non-vanishing viscosity, however, the viscous friction at the boundaries of the horseshoe region (the separatrices) enables a steady flux of angular momentum across the horseshoe region, and the asymptotic value of the horseshoe drag may remain finite. It is the purpose of this paper to provide the asymptotic value of the torque.

An estimate of the saturated horseshoe drag already exists in the literature (Masset 2001), but it applies exclusively to isothermal (or barotropic) disks, that is to say to disks in which the pressure is solely a function of the density. It has recently been shown that the horseshoe dynamics is more complex in non-isothermal flows, which obey an energy equation rather than a barotropic closure relation (Paardekooper & Mellema 2006; Baruteau & Masset 2008; Paardekooper & Papaloizou 2008; Masset & Casoli 2009; Paardekooper et al. 2009).

In any case, the key quantity that determines the value of the horseshoe drag is the vortensity, or potential vorticity. It is the value of the vertical component of the vorticity divided by the surface density of the disk. Regardless of the equation of state, the horseshoe drag always reduces to a simple integral involving the vortensity distribution across the horseshoe region. In a non-isothermal flow, baroclinic effects act as source or sink terms for the vortensity, which in turn has a strong im-

pact on the horseshoe drag. These effects have been found to be localized exclusively at the separatrices of the horseshoe region (Masset & Casoli 2009), and they scale with the entropy gradient in the disk. As entropy follows the horseshoe streamlines and tends to be flattened over the horseshoe region by phase mixing, the entropy gradient that persists over long time scales across the horseshoe region depends on diffusive processes that affect the evolution of entropy (such as thermal diffusion, and in a more general manner all the processes that act as sink or source terms in the energy equation). The asymptotic torque expression therefore involves two main dissipative processes: viscosity, and thermal diffusion, and it depends on two gradients: the gradient of vortensity, and the gradient of entropy.

As a point of terminology, we mention that the component of the horseshoe drag which scales with the vortensity gradient has been called vortensity-related torque (Paardekooper et al. 2009), or bulk term (Masset & Casoli 2009), whereas its additional non-barotropic component has been called entropy-related torque (Paardekooper et al. 2009), edge term (Masset & Casoli 2009), or adiabatic torque excess (Masset & Casoli 2009; Baruteau & Masset 2008). We will use indifferently these denominations, but we shall reserve the last one for the unsaturated horseshoe drag, for which the dissipative processes are unimportant and the flow can be considered as adiabatic.

This paper is organized as follows: section 2 presents the framework and introduces the notation and governing equations, section 3 presents a reduced model of the flow that retains its essential characteristics for the horseshoe dynamics, section 4 presents a derivation of the horseshoe drag expression that we shall use to get the asymptotic estimates. This expression is strictly equivalent to the expression of Masset & Casoli (2009), in which the edge term is now incorporated into the integral over the vortensity, which is singular at the separatrix. In section 5, we present the set of full hydrodynamical simulations that we have performed with the FARGO code, and we compare their results with those of the reduced model of section 3. In section 6, we work out suitable relationships for the steady state flow, and infer the corresponding asymptotic horseshoe drag. Our analysis is exact in the limit of small viscosity or small thermal diffusion, but its overall accuracy is found to be satisfactory up to the values for which the torque remains fully unsaturated. For the convenience of the reader mainly interested in the results and their implementation, section 8 is self-contained (the notation required to follow that section is given in Tab. 1). It provides the torque value as a function of viscosity and thermal diffusivity for low-mass planets subject to type I migration. Section 9 provides additional discussion, and we draw our conclusions in section 10.

## 2. PREREQUISITE

### 2.1. Framework

A fundamental premise of our analysis is that a turbulent protoplanetary disk can be adequately modeled by a laminar, non-magnetized disk, in which diffusion (of energy and angular momentum) is described by phenomenological diffusion coefficients. Turbulence,

which likely results from the magnetorotational instability (Balbus & Hawley 1991), acts at exchanging angular momentum across the horseshoe separatrices. We assume that it does so in a diffusive manner on the radial scale of the horseshoe region. It is not clear whether this is the case for the low or intermediate mass planets considered here, for which the horseshoe zone width is at most of the order of the disk thickness, that is to say of same order than the largest scale of the turbulence. Since this is a totally unexplored regime, which awaits dedicated three dimensional MHD calculations, we shall restrict ourselves to this assumption so that it can be modeled by resorting to the Navier Stokes equation with an effective kinematic viscosity. Little is known on the validity of this assumption in the context of horseshoe drag saturation. Nevertheless, we mention the encouraging results of Baruteau & Lin (2010), who have considered an inviscid two-dimensional disk subject to stochastic forcing, and found saturation properties of the horseshoe drag very similar to those in a laminar disk.

In this picture the details of the properties of turbulence should not matter. The scale at which the turbulent cascade dissipates (resistive or viscous) may impact the saturated state of the turbulence, i.e. the value of the effective viscosity (see Fromang et al. 2010, and refs. therein). However, provided the correct value of the effective viscosity is used, the time averaged distribution of vortensity within the horseshoe region should be insensitive to the statistical properties of the turbulence.

We note that all what matters to assess the asymptotic horseshoe drag is how much angular momentum exchange subsists at large time between the disk and the horseshoe region, considered here in a wide meaning as everything enclosed within the separatrices, including the planet (e.g. Masset 2001). For this reason, the horseshoe drag is always linked to the flow properties at the separatrices. The internal details of the coorbital flow, such as the existence of tadpole streamlines or the topology of the flow in the vicinity of the planet, do not impact the horseshoe drag. Stated differently, since the whole set of librating material is trapped in the coorbital region and migrates along with it (e.g. Masset & Papaloizou 2003), the forces internal to the horseshoe region are internal to the migrating system and therefore do not affect its migration rate.

Turbulence also yields a stochastic torque that triggers a random walk of the semi-major axis of the planet (Nelson 2005), which comes in addition to the systematic drift due to the wake. As a consequence the probability density of the planet's semi-major axis obeys a diffusion-advection law (Johnson et al. 2006). When averaging over a sufficient amount of time, the systematic drift overcomes the stochastic effects. Although it is still unclear whether the drift so averaged amounts to the drift obtained from a laminar analysis (Nelson 2005), we assume here that this is the case, and that the long-term effects of turbulence exclusively amount to regulating the degree of saturation of the horseshoe region, from which we infer laminar torque values which dictate the time averaged migration rate.

In a similar vein, a number of different processes, in addition to turbulence itself, lead to a diffusion of temperature in the disk, such as thermal diffusion or radiative diffusion, while cooling through the disk's photosphere and

heating by turbulence also contribute to the energy budget. For the sake of simplicity, we shall assume that the time evolution of the fluctuations of temperature with respect to the unperturbed state can be described by a unique diffusion coefficient, to which we refer as the thermal diffusivity, which is an effective diffusion coefficient much as the effective viscosity. This is a rather standard practice (e.g. Paardekooper & Papaloizou 2008). We shall see that all what matters to determine the degree of saturation of the entropy related torque is the entropy difference on both separatrices upstream of the U-turns, and that the only parameter that determines this difference is the ratio of the thermal timescale to the horseshoe libration timescale. Our simplifying assumption therefore retains all the physics relevant to the description of the saturation of the non-isothermal horseshoe drag.

Finally, most of our study (analytical and numerical) is performed assuming a two-dimensional disk, for reasons of tractability and computational cost. In section 7.2.1 we will try and generalize to three dimensions in the framework of stacked two dimensional layers.

## 2.2. Notation

In addition to the notation defined below, the notation used in section 8 is presented in table 1, for the convenience of the reader mainly interested in the results presented in that section. We consider a planet of mass  $M_p$  orbiting a star of mass  $M_*$ , on a fixed circular orbit. This planet is embedded in a gaseous protoplanetary disk, such that the planetary orbit is coplanar with the disk and prograde. We use  $P$  to denote the vertically integrated pressure, and  $s$  to denote the gas entropy, which reads:

$$s = \frac{P}{\Sigma\gamma}, \quad (1)$$

where  $\Sigma$  and  $\gamma$  are defined in Tab. 1.

We identify a location in the disk by its distance  $r$  to the star and its azimuth  $\phi$  with respect to the planet. The gas has a radial velocity  $v_r$  and an azimuthal velocity  $v_\phi$  in the frame corotating with the planet (hence its angular frequency in an inertial frame is  $\Omega = v_\phi/r + \Omega_p$ ). The radius of corotation  $r_c$  is the location in the unperturbed disk where the material has same angular frequency as the planet:  $\Omega(r_c) = \Omega_p$ . We will make use of the distance  $x$  to corotation:  $x = r - r_c$ . We also consider the disk pressure scaleheight  $H = c_s/\Omega = rh$ .

We denote with a subscript 0 the value of a variable in the unperturbed disk, and with a subscript 1 the perturbation of this variable. Whenever we refer to the unperturbed value of a variable at corotation, we use a  $c$  subscript.

Using the notation of Baruteau & Masset (2008), we define the gradient of the inverse of vortensity across corotation as:

$$\mathcal{V} = \left. \frac{d \log(\Sigma_0/\omega_0)}{d \log r} \right|_c = \frac{3}{2} + \frac{r_c}{\Sigma_c} \left. \frac{d\Sigma_0}{dr} \right|_{r_c} = \frac{3}{2} - \alpha, \quad (2)$$

where  $\alpha$  is the index of the surface density power law (see Tab. 1), and where  $\omega = (1/r)\partial_r(r^2\Omega)$  is the vertical component of the flow vorticity. We will also make use of the first Oort's constant  $A = (1/2)r d\Omega/dr$ , which

**Table 1**  
Main notation used in this work.

Name	Notation	Comment
Planet orbital frequency	$\Omega_p$	
Planet semi major axis	$a$	
Planet to star mass ratio	$q$	$q = M_p/M_*$
Disk surface density	$\Sigma$	$\Sigma = \Sigma_c(r/a)^{-\alpha}$
Vertically averaged temperature	$T$	$T = T_c(r/a)^{-\beta}$
Flaring Index	$f$	$f = (1 - \beta)/2$ $h \propto r^f$
Disk aspect ratio	$h$	$h = h_0(r/a)^f$
Vortensity gradient	$\mathcal{V}$	$\mathcal{V} = 3/2 - \alpha$
Adiabatic index	$\gamma$	
Entropy gradient	$\mathcal{S}$	$\mathcal{S} = \frac{\gamma-1}{\gamma}\alpha + \frac{2f-1}{\gamma}$ The entropy scales as $r^{\gamma\mathcal{S}}$
Horseshoe half width	$x_s$	

**Note.** — The entropy gradient  $\xi$  defined by Paardekooper et al. (2009) is equivalent to  $\gamma\mathcal{S}$ .

quantifies the amount of shear in the unperturbed flow, and of the second Oort's constant  $B = (1/2r)d(r^2\Omega)/dr$ , which is half the vertical component of the unperturbed flow's vorticity. Instead of the vortensity  $w$  defined by  $w = \omega/\Sigma$ , we oftentimes consider its inverse  $l = 1/w$ , that we call the load for the sake of definiteness:  $l = \Sigma/\omega$ . We define the gradient of entropy across corotation as:

$$\mathcal{S} = \frac{1}{\gamma} \frac{d \log s_0}{d \log r} \Big|_c. \quad (3)$$

We shall make use of the dimensionless variables

$$L = (l - l_c)/l_c \quad \text{and} \quad S = (s - s_c)/s_c. \quad (4)$$

We denote the slope of these variables in the unperturbed disk respectively with  $L'_\infty$  and  $S'_\infty$ , where the prime stands for the derivative with respect to  $x$ . We have the following relationships:

$$L'_\infty = \frac{\mathcal{V}}{a} \quad (5)$$

$$S'_\infty = \frac{\gamma\mathcal{S}}{a}. \quad (6)$$

The reason for the  $\infty$  symbol in the expressions above will appear in section 3.3. They represent the large scale gradient in the unperturbed disk, and therefore the asymptotic value of the slope of the load or entropy as one goes away from the corobital region.

### 2.3. Governing equations

The governing equations of the flow are the equation of continuity, the Navier-Stokes equations and the energy equation, together with the closure relationship provided by the equation of state, which is that of an ideal gas:

$$P = \mathcal{R}\Sigma T/\mu, \quad (7)$$

where  $\mathcal{R}$  is the ideal gas constant and  $\mu$  the mean molecular weight of the gas. The equation of continuity reads, in the frame corotating with the planet:

$$\partial_t \Sigma + \frac{1}{r} \partial_r (\Sigma r v_r) + \frac{1}{r} \partial_\phi (\Sigma v_\phi) = 0. \quad (8)$$

The Navier-Stokes equations read, respectively in the radial and azimuthal directions:

$$\partial_t v_r + v_r \partial_r v_r + \frac{v_\phi}{r} \partial_\phi v_r - r \Omega_p^2 - 2\Omega_p v_\phi - \frac{v_\phi^2}{r} = -\frac{\partial_r P}{\Sigma} - \partial_r \Phi + \frac{f_r}{\Sigma}, \quad (9)$$

and:

$$D_t j = -\frac{\partial_\phi P}{\Sigma} - \partial_\phi \Phi + \frac{r f_\phi}{\Sigma}, \quad (10)$$

where  $D_t \equiv \partial_t + v_r \partial_r + \frac{v_\phi}{r} \partial_\phi$  and

$$j = r^2 \Omega \quad (11)$$

is the specific angular momentum. In Eqs. (9) and (10),  $f_r$  and  $f_\phi$  are respectively the radial and azimuthal component of the viscous force per unitary surface. These viscous forces are derived from the viscous stress tensor as follows:

$$f_r = \frac{1}{r} \frac{\partial(r\tau_{rr})}{\partial r} + \frac{1}{r} \frac{\partial\tau_{r\phi}}{\partial\phi} - \frac{\tau_{\phi\phi}}{r} \quad (12)$$

$$f_\phi = \frac{1}{r} \frac{\partial(r\tau_{\phi r})}{\partial r} + \frac{1}{r} \frac{\partial\tau_{\phi\phi}}{\partial\phi} + \frac{\tau_{r\phi}}{r}, \quad (13)$$

where the components of the viscous stress tensor are:

$$\tau_{rr} = 2\eta D_{rr} - \frac{2}{3}\eta \nabla \cdot \mathbf{v} \quad (14)$$

$$\tau_{\phi\phi} = 2\eta D_{\phi\phi} - \frac{2}{3}\eta \nabla \cdot \mathbf{v} \quad (15)$$

$$\tau_{r\phi} = \tau_{\phi r} = 2\eta D_{r\phi}, \quad (16)$$

where

$$D_{rr} = \frac{\partial v_r}{\partial r}, D_{\phi\phi} = \frac{1}{r} \frac{\partial v_\phi}{\partial\phi} + \frac{v_r}{r} \quad (17)$$

$$D_{r\phi} = \frac{1}{2} \left[ r \frac{\partial}{\partial r} \left( \frac{v_\phi}{r} \right) + \frac{1}{r} \frac{\partial v_r}{\partial\phi} \right], \quad (18)$$

and  $\eta = \Sigma\nu$  is the vertically integrated dynamical viscosity coefficient. The internal energy density is  $e = p/(\gamma - 1)$ , and the energy equation reads:

$$\Sigma D_t \left( \frac{e}{\Sigma} \right) = -p \vec{\nabla} \cdot \vec{v} - \vec{\nabla} \cdot \vec{F}, \quad (19)$$

where the last term of the right hand side accounts for the energy diffusion, and will be given explicitly in section 2.5.

#### 2.4. Time evolution of the load

The evolution of the load or vortensity that the material undergoes in the coorbital region corresponds to a slow transformation which takes place while the fluid elements describe essentially circular trajectories, far from the planet, between successive horseshoe U-turns. We therefore neglect the azimuthal derivatives in the equation governing the evolution of the load. Eq. (10) can then be recast as:

$$\partial_t j + v_r r \omega = \frac{1}{r \Sigma} \partial_r (r^2 \tau_{\phi r}), \quad (20)$$

where we have used (11), (13) and (16). Deriving with respect to  $r$ , using Eq. (8) and (18), we are left with:

$$D_t w = \frac{1}{r \Sigma} \partial_r \left[ \frac{1}{r \Sigma} \partial_r (\Sigma \nu r^3 \partial_r \Omega) \right]. \quad (21)$$

We assume that  $\nu$  is a power law of radius, such that the inner bracket of Eq. (21) is flat in an unperturbed disk, which amounts to assuming that there is no radial drift of material. We mention that, in some of our numerical simulations, we have precisely adopted such a prescription (see section 5.3.2). We can thus write, keeping only the highest order derivatives of the perturbed quantities:

$$D_t w \approx \nu \partial_{r^2}^2 w_1 - 2\nu w_0 \frac{\partial_{r^2}^2 \Sigma_1}{\Sigma_0}, \quad (22)$$

where  $\Omega_0$  and  $\Sigma_0$  are respectively the angular velocity and surface density of the unperturbed disk, whereas  $\Omega_1$  and  $\Sigma_1$  are the perturbations of azimuthal velocity and surface density. In Eq. (22) we have made use of the first order expansion:

$$w_1 \approx r \frac{\partial_r \Omega_1}{\Sigma_0} - \frac{w_0}{\Sigma_0} \Sigma_1, \quad (23)$$

and of the relationship, specific to Keplerian disks:

$$\partial_r \Omega_0 = -3 \frac{w_0 \Sigma_0}{r}. \quad (24)$$

Recasting Eq. (22) in terms of the load, we obtain:

$$D_t l \approx \nu \partial_{r^2}^2 l + 2\nu l_0 \frac{\partial_{r^2}^2 \Sigma}{\Sigma_0}, \quad (25)$$

where we have used the relationships  $\partial_{r^2}^2 l_1 \approx \partial_{r^2}^2 l$  and  $\partial_{r^2}^2 \Sigma_1 \approx \partial_{r^2}^2 \Sigma$ . The typical value of the perturbed load in the horseshoe region is indeed  $O(l_c x_s / a)$ , whereas it varies radially over a length scale at most equal to  $x_s$ . The same applies to the surface density, except in a barotropic disk: we note that if the radial scale of the disturbances in the disk is small with respect to the pressure scale length (i.e. with respect to the disk thickness), then, in a barotropic disk, the excitation of evanescent pressure waves renders the relative perturbation of surface density much smaller than the relative perturbation of vortensity or load (Casoli & Masset 2009), so that the perturbation of vortensity can be put solely on the account of the perturbation of vorticity, and Eq. (25) can

then be recast as:

$$D_t l \approx \nu \partial_{r^2}^2 l. \quad (26)$$

On the contrary if the pressure length scale is shorter than the radial scale of the disturbances, then the acoustic spread of the perturbations does not significantly alter the perturbations of surface density, so that the relative perturbation of load is equal to the relative perturbation of surface density. In that case, Eq. (25) yields:

$$D_t l \approx 3\nu \partial_{r^2}^2 l. \quad (27)$$

In the case that we contemplate in this work, that of a low-mass planet embedded in a disk, for which the half-width of the horseshoe region is smaller than the disk thickness (Masset et al. 2006), the regime that prevails corresponds to Eq. (26). Eq. (27) would be valid for very massive protoplanets, but it would be of little interest, since those clear a gap in their coorbital region, thereby shutting off the corotation torque.

We note that in a non-barotropic disk, in which there can be entropy waves and therefore contact discontinuities, the last term of Eq. (25) may no longer be negligible. This is in particular the case at the outer edge of the horseshoe region, downstream of the U-turns (Masset & Casoli 2009). We shall therefore use Eq. (26) for barotropic disks, and Eq. (25) for disks with an energy equation.

#### 2.5. Time evolution of the entropy

Using Eq. (7) we can transform Eq. (19) into:

$$\frac{\mathcal{R} \Sigma T}{(\gamma - 1) \mu} D_t \log s = -\vec{\nabla} \cdot \vec{F}, \quad (28)$$

where  $\vec{F}$  is the heat flux, given by:

$$F = -k \nabla T, \quad (29)$$

where  $k$  is the thermal diffusivity. Assuming that it can be regarded as constant over the length scales over which  $T$  varies, Eq. (28) can be recast as:

$$\frac{\mathcal{R} \Sigma T}{(\gamma - 1) \mu} D_t \log s = k \Delta T. \quad (30)$$

We now note that, for the case we are interested in, that of a horseshoe region bound by contact discontinuities, the variations of temperature occur on a much smaller scale than those of pressure, which occur on the disk scale height. We therefore make the following simplifying assumption, using Eq. (1):

$$\frac{\Delta T}{T} = \frac{1}{\gamma} \frac{\Delta s}{s}. \quad (31)$$

Using Eqs. (30) and (31), we are led to:

$$D_t s = \kappa \Delta s, \quad (32)$$

where

$$\kappa = \frac{\gamma - 1}{\gamma} \frac{k \mu}{\mathcal{R} \Sigma}. \quad (33)$$

The simplifying assumption underlying Eq. (31) has several important properties:

- Our prescription for thermal diffusion has no impact on the acoustic waves, since the diffusion term scales with the perturbations of entropy, which vanish in acoustic waves. It has therefore no impact on the differential Lindblad torque, and allows to disentangle in a clean manner the variations of the corotation torque due to variations of thermal diffusion.
- Eq. (32) shows that the evolution of entropy does not depend on other variables, if we regard  $\Sigma$  as a constant, and if we consider that the streamlines do not depend on the perturbation that builds up in the coorbital region. Finding a steady state solution for the coorbital flow can therefore be done in two subsequent steps: (i) one first seeks a steady state solution for the entropy, which does not require the knowledge of any other variable, (ii) one then seeks a steady state solution of the vortensity, as the latter depends on the entropy field, in a manner that shall be specified in the next section.

We comment that we have undertaken a side study of the variation of the Lindblad torque as the thermal diffusivity varies (see section 7.1) using the alternate form of the diffusion term (which then scales with the Laplacian of the temperature, rather than the entropy). The transition of the Lindblad torque from the adiabatic limit to the isothermal limit (the respective torque values differ by a factor  $\gamma$ ) occurs for values of the thermal diffusion much larger than those relevant for the saturation of the entropy related corotation torque.

### 3. A SIMPLIFIED MODEL OF THE FLOW

#### 3.1. Simplifying assumptions

Owing to the complexity of the coorbital flow of an embedded planet, we have to make a number of simplifying assumptions which render tractable the task of finding the expression of the steady state horseshoe drag. We anticipate that these assumptions do not impact significantly the horseshoe drag expression. We will check this in section 5.4.

- We separate the time scales of the horseshoe U-turns and that of the drift between two successive U-turns (i.e. half the libration time scale). The former is at least one order of magnitude shorter than the latter (Baruteau & Masset 2008). This allows us to consider that the horseshoe U-turns are performed instantaneously.
- Similarly, we consider that the azimuthal interval over which the U-turns take place is small compared to  $2\pi$ . This amounts to considering that the U-turns are squeezed against the axis joining the star and the planet.
- We assume that the vortensity (or load) is conserved during the U-turns, except for the stagnation streamline (separatrix) in the non barotropic case, at which a singular amount of vortensity is created (Masset & Casoli 2009). Note that some vortensity is created during the U-turns in a non barotropic flow (Masset & Casoli 2009) for all

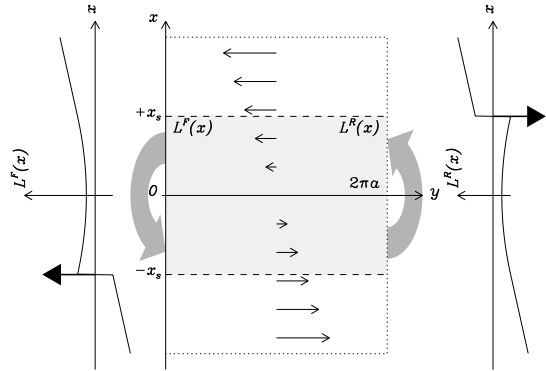


**Figure 1.** Sketch of the flow and of the load profile in front and behind the planet, within our simplified framework. The graphs on the left and right side present a sketch of the front and rear load profiles, respectively. The thick arrows in these graphs represent the singular load on the downstream separatrix. The light shaded area enclosed within the horizontal dashed lines shows the horseshoe region. The functions  $L^F(x)$  and  $L^R(x)$  are even for  $x \in [-x_s, x_s]$ . The central set of arrows depicts the Keplerian flow, for which  $v_y = 2Ax$ .

streamlines, but this has no impact on the horseshoe drag, hence we disregard it in this analysis. Also, the vortensity is ill-defined at the downstream separatrix, where there is both a contact discontinuity and a vorticity sheet. Nevertheless, the contact discontinuity has a surface density jump which is first order in  $x_s/a$  (Baruteau & Masset 2008), hence to lowest order in  $x_s/a$  the singularity of vortensity can be defined as  $\Delta v_\phi \delta(x - x_s)/\Sigma_0$ , where  $\Delta v_\phi$  is the jump of azimuthal velocity across the downstream separatrix.

- We assume that the streamlines can be regarded as circular between two U-turns. This amounts to neglecting the radial velocity in the coorbital region, and to disregarding the behavior induced by the indirect term of the potential.
- We assume that the U-turns are symmetric, i.e. that a streamline which has a radius  $r$  prior to a U-turn is mapped to a streamline with radius  $2r_c - r$ , its distance to corotation remaining therefore  $|r - r_c|$ .

A consequence of this set of assumptions is that the path followed by a horseshoe fluid element in the  $(y, x)$  plane is rectangular (where  $y = r\phi$ ), and that the load and entropy are even functions of  $x$  over the interval  $[-x_s, x_s]$  in  $\phi = 0$  (front U-turns) and in  $\phi = 2\pi$  (rear U-turns), except for the possible creation of a singular amount of load in  $x = \pm x_s$ . Hereafter we will write with a superscript  $F$  ( $R$ ) the quantities in  $y = 0^+$  ( $y = 2\pi a^-$ ) so as to remind that they are evaluated in front (at the rear) of the planet. A generic situation for the load is represented in Fig. 1.

#### 3.2. Governing equations of the reduced model

In the framework considered in the previous section, we consider a restricted model of the flow, in which we have only one scalar field in the barotropic case (the load) or two scalar fields in the case with an energy equation: the load and the entropy. In the barotropic case, the variable

$L$  obeys an equation derived from Eq. (26), which reads in the framework of the reduced model:

$$\partial_t L + 2Ax\partial_y L = \nu L''. \quad (34)$$

In the case with an energy equation, the variable  $L$  obeys an equation similar to Eq. (25). The radial scale for the variation of pressure is much larger than the scale of variation of entropy or surface density, so we are led to:

$$\partial_t L + 2Ax\partial_y L = \nu L'' - \frac{2\nu}{\gamma} S''. \quad (35)$$

In this case, we also need to consider the time evolution of the entropy. Eq. (32) yields:

$$\partial_t S + 2Ax\partial_y S = \kappa S''. \quad (36)$$

Eqs. (34) to (36) amount to considering exclusively the radial diffusion of these quantities, and to assuming that the underlying flow is the unperturbed Keplerian flow, rectified on a Cartesian slab.

### 3.3. Boundary conditions of the reduced model

The boundary conditions of this reduced model are periodic in  $y$  outside of the horseshoe region, with a period equal to  $2\pi a$ , that is to say:

$$L^F(x) = L^R(x) \text{ and } S^F(x) = S^R(x) \text{ for any } x \text{ such that } |x| > \pi a \quad (37)$$

whereas within the horseshoe region the following relationships hold:

$$L^F(x) = L^F(-x) + L_0\delta(x + x_s) \text{ for any } x \in [-x_s, 0] \quad (38)$$

$$L^R(x) = L^R(-x) - L_0\delta(x - x_s) \text{ for any } x \in [0, x_s] \quad (39)$$

and

$$S^F(x) = S^F(-x) \text{ for any } x \in [-x_s, x_s] \quad (40)$$

$$S^R(x) = S^R(-x) \text{ for any } x \in [-x_s, x_s] \quad (41)$$

Eqs. (38) and (39) are meant to account for the horseshoe U-turns, in which the load is conserved, except at the downstream separatrices where a singular amount  $\pm\Lambda_0 = L_0 l_c$  is created, as has been shown by Masset & Casoli (2009), and as we shall discuss more in detail in section 4. The entropy obeys similar equations, except that it is conserved during the U-turns, even at the separatrix.

In the  $x$  direction, boundary conditions are set for  $|x| \rightarrow \infty$  such that the slopes of the fields  $L$  and  $S$  are that of the unperturbed flow:

$$\lim_{x \rightarrow \pm\infty} \partial_x L(x, y) = L'_\infty \text{ for any } y \in [0, 2\pi a] \quad (42)$$

and

$$\lim_{x \rightarrow \pm\infty} \partial_x S(x, y) = S'_\infty \text{ for any } y \in [0, 2\pi a] \quad (43)$$

### 3.4. Symmetry of the reduced model

The reduced model exhibits the following symmetry:

$$L(x, y) = -L(-x, 2\pi a - y). \quad (44)$$

while a similar property holds for the entropy field. The system is set with this symmetry at  $t = 0$ , since  $L(x, y) \propto x$  in the unperturbed flow, and the governing

equation (34) as well as the boundary conditions specified by Eqs. (37) to (39) ensure that Eq. (44) holds at any time. As a consequence we have:

$$L^R(-x) = -L^F(x) \text{ for any } x \quad (45)$$

and

$$S^R(-x) = -S^F(x) \text{ for any } x \quad (46)$$

### 3.5. General considerations on the steady state of the reduced model

The scalar field  $S$  is not subject to any feed back from  $L$ : it evolves by itself. On the contrary, the singular vortensity  $\pm\Lambda_0$  created at the downstream separatrices is linked to a difference of the value of the entropy at the upstream front and rear separatrices (Masset & Casoli 2009). We have, using Eq. (62) of Masset & Casoli (2009):

$$\Lambda_0 = -\frac{\Sigma_0 \Delta v}{(2B)^2} = \frac{\Gamma_1}{16a|A|x_s^2 B^2}, \quad (47)$$

where  $\Gamma_1$ , the adiabatic torque excess, has been worked out by Masset & Casoli (2009) [see e.g. their Eq. (96)], and where  $\Delta v$  is the azimuthal velocity jump across the downstream separatrix. In an unsaturated situation,  $\Gamma_1$  (and therefore  $\Lambda_0$ ) depend on the unperturbed entropy gradient  $\mathcal{S}$  in the disk, which imposes the entropy difference at the upstream separatrices. In a saturated situation, the latter must be substituted by the effective entropy gradient, which depends on the actual value of the entropy difference at the upstream separatrices (rather than the unperturbed one):

$$S' = \frac{1}{\gamma} \frac{a}{s_c} \frac{s^F(x_s) - s^R(-x_s)}{2x_s} = \frac{1}{\gamma} \frac{a}{x_s} S^F(x_s), \quad (48)$$

where we have used the symmetry property of Eq. (46). The steady state situation is therefore determined as follows:

- A steady state solution is sought for the entropy field  $S$ .
- Using Eq. (48), this solution is used to evaluate  $\Gamma_1$  and therefore  $\Lambda_0$ , the production of vortensity at the downstream separatrix.
- Once  $\Lambda_0$  is known, one can determine a steady state solution for the load field  $L$ .
- The latter can then be used to evaluate the horseshoe drag as explained in section 4.

### 3.6. Implementation of the reduced model

The reduced model presented above can be easily implemented as a simple grid-based code. It allows to get values of the asymptotic horseshoe drag at low computational cost. Namely, we solve the evolution equations (34) and (36) on a mesh subdivided in  $N_x \times N_y$  zones. The advection of the field (either load or entropy) can be ensured by any upstream TVD scheme (in our case we use a monotized centered slope limiter). The timestep is limited by the Courant criterion, which reads here:

$$\Delta t = C_0 \min[(\Delta t_1^{-2} + \Delta t_2^{-2} + \Delta t_3^{-2})^{-1/2}], \quad (49)$$

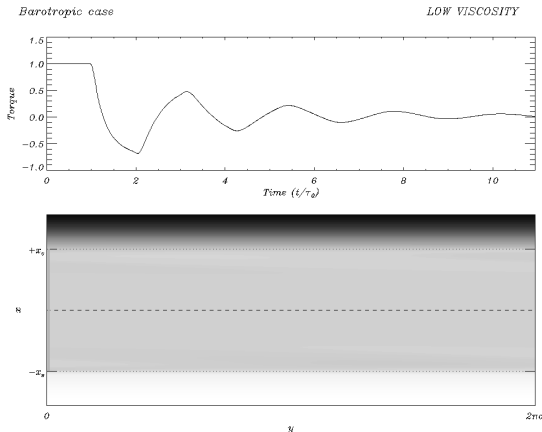


**Figure 2.** Still frame of the animation, that shows the load distribution at the end of the calculation (bottom) and the horseshoe drag as a function of time, in arbitrary units (top). The viscosity is low in this case, so that the load distribution eventually becomes flat. The animations shows two additional cases: a high viscosity case, in which the torque levels off to a non-vanishing value, and a case with an energy equation (i.e. the appearance of singular load sheets at the downstream separatrices) in which the torque oscillates and eventually decays to a rather low value.

where  $\Delta t_1 = \Delta x^2/(2\nu)$ ,  $\Delta t_2 = \Delta x^2/(2\kappa)$ ,  $\Delta t_3 = \Delta y/|2Ax|$ ,  $\Delta x$  and  $\Delta y$  being the mesh resolution respectively in  $x$  and  $y$  ( $\Delta x \ll \Delta y$ ). In Eq. (49) we chose the Courant number  $C_0 = 0.9$ , and the min operator is meant to be taken for all the zones. The quadratic sum that features in Eq. (49) is similar to that in Eq. (74) of Stone & Norman (1992).

The diffusion either of load or entropy is implemented by a second order explicit operator, in the  $x$  direction only. The corresponding substep therefore reads, for the load:

$$L_{ij}^b = L_{ij}^a + \nu \Delta t \frac{L_{i+1j}^a + L_{i-1j}^a - 2L_{ij}^a}{\Delta x^2}, \quad (50)$$

where  $i$  and  $j$  are the zone indexes respectively in  $x$  and  $y$ , and where the  $a$  and  $b$  superscripts denote the load respectively before and after the diffusion substep.

The mesh is designed so that the corotation and both separatrices fall on the interface between adjacent rows of zones. The horseshoe region therefore covers an integer and even number of rows. One column of ghost zones is used on each side in  $y$ . For the zones of the inner or outer disk, standard periodic boundary conditions are applied in order to set the values in the ghost zone. For the rows which are within the horseshoe region, the boundary conditions differ, so as to mimic the U-turns. An animation of the time dependent load distribution is available in a separate file. Fig. 2 shows a still frame extracted from this animation, which also displays the corresponding horseshoe drag value. The manner in which the latter is estimated is detailed in the next section.

#### 4. HORSESHOE DRAG EXPRESSION

We use the horseshoe drag expression given by Masset & Casoli (2009), which we transform so that the entropy related torque (corresponding to the last term of this equation) feature the load produced during the U-turns. The horseshoe drag expression given at Eq. (37)

by Masset & Casoli (2009) can be recast as:

$$\Gamma = \Gamma^F + \Gamma^R, \quad (51)$$

where the superscripts  $F$  and  $R$  respectively stand for the front and rear contribution to the horseshoe drag, which read respectively:

$$\Gamma^F = \int_{G_s}^{G_c} l_+ \Delta j_0 dG - \frac{\Sigma_0}{4B} \Delta j_0^s \Delta G \quad (52)$$

$$\Gamma^R = - \int_{G_s}^{G_c} l_- \Delta j_0 dG - \frac{\Sigma_0}{4B} \Delta j_0^s \Delta G, \quad (53)$$

where  $G$  is defined at Eq. (16) of Masset & Casoli (2009), and where  $\Delta j_0 = 4aBx$  is the jump of specific angular momentum of fluid elements that execute a U-turn from  $r = a+x$  to  $r = a-x$ , while  $\Delta j_0^s$  refers to the same quantity for  $x = x_s$ . Note that we have split the torque excess (trailing term of Eq. (37) in MC09) into a front part and a rear part, which are equal for symmetry reasons. Using Eqs. (19), (37) and (62) of Masset & Casoli (2009), one can recast the front contribution to the horseshoe drag as an integral over  $0 < x < x_s$ , corresponding to the streamlines which undergo a horseshoe U-turn towards smaller radii in front of the planet:

$$\Gamma^F = \int_0^{x_s} 4|A|Bl^F(x)\Delta j_0 x dx + 2|A|B\Lambda_0\Delta j_0^s x_s, \quad (54)$$

By convention, Eq. (54) and all the torque expressions that we shall write correspond to the torque exerted by the disk onto the planet. From the definition of  $\Delta j_0$  it follows that it is a positive quantity on the interval considered, and that  $\Gamma^F$  is also positive, as expected since it stems from material in front of the planet. In Eq. (54), the trailing term comes from the torque excess expression given by Eq. (37) of Masset & Casoli (2009), that we have transformed using Eq. (47). We recast Eq. (54) as:

$$\Gamma^F = 16|A|B^2a \int_0^{x_s} l^F(x)x^2 dx + 8|A|B^2a\Lambda_0x_s^2, \quad (55)$$

We transform Eq. (55) using Eq. (38), which allows to embed the singular contribution within the integral:

$$\Gamma^F = 8|A|B^2a \int_{-x_s}^{x_s} l^F(x)x^2 dx. \quad (56)$$

In this equation the integrand is singular in  $x = -x_s$ , that is to say at the edge of the integration domain. It is therefore necessary to specify explicitly how to deal with this singular contribution. Comparison of Eqs. (55) and (56) shows that one must take into account the whole singular distribution in the integral (as if it was approximated by a narrow function whose support was entirely contained within the interval of integration). Hereafter, whenever we shall consider a horseshoe drag-like integral, with an integrand singular on an edge (i.e. at a separatrix), we shall implicitly consider that all the singularity must be taken into account in the integral.

The rear contribution to the horseshoe drag can be worked out in a similar manner and reads:

$$\Gamma^R = -8|A|B^2a \int_{-x_s}^{x_s} l^R(x)x^2 dx, \quad (57)$$



where, again,  $L^R(x)$ , the load at the rear of the planet, may contain a singular contribution in  $x = x_s$ , arising from the production of load during the U-turn. The whole horseshoe drag therefore reads:

$$\Gamma = 4|A|Ba\Sigma_0 \int_{-x_s}^{x_s} [L^F(x) - L^R(x)]x^2 dx, \quad (58)$$

This expression can be further simplified, using Eq. (45), as:

$$\Gamma = 8|A|B\Sigma_0 a \int_{-x_s}^{x_s} L^F(x)x^2 dx, \quad (59)$$

Simple particular cases can be recovered from Eq. (59):

- In the unsaturated barotropic case with a vortensity gradient  $\mathcal{V} = aL'_\infty$ , we have  $L^F(x) = \mathcal{V}x/a$ , from which we infer:

$$\Gamma = 4|A|B\Sigma_0 \mathcal{V}x_s^4, \quad (60)$$

or:

$$\Gamma = \Gamma_0 \mathcal{V}, \quad (61)$$

which is the standard barotropic horseshoe drag expression (Ward 1991; Masset 2001), where

$$\Gamma_0 = \frac{3}{4}\Sigma_0 \Omega^2 x_s^4, \quad (62)$$

if we specialize to the case of a Keplerian disk.

- In an inviscid barotropic disk in steady state in the corotating frame, the load is conserved along a streamline, hence  $L^F(x) = L^R(x)$ . Since  $L^R(x) = L^R(-x) = -L^F(x)$ , we infer that  $L^F(x) = 0$  for any  $x \in [0, x_s]$ . The horseshoe drag therefore cancels out. It is fully saturated, and the load is profile is flat across the horseshoe region.
- In an adiabatic flow without vortensity gradient, the only contribution to the integrand stems from the singularity  $\Lambda_0$  at the downstream separatrix, which leads to:

$$\Gamma = 16|A|B^2 a x_s^2 \Lambda_0, \quad (63)$$

which, using Eq. (47), yields  $\Gamma = \Gamma_1$ .

## 5. NUMERICAL SIMULATIONS

In addition to the calculations performed with the reduced model presented in section 3, we have performed three series of full hydrodynamical simulations. We describe hereafter the code and the different setups that we have adopted.

### 5.1. Code and setup

We have used the hydrocode FARGO<sup>3</sup> in its isothermal version (Masset 2000a,b) and in its adiabatic version (Baruteau & Masset 2008; Baruteau 2008). The FARGO code is a staggered mesh hydro-code on a polar grid, with upwind transport and a harmonic, second order slope limiter (van Leer 1977). It solves the Navier-Stokes and continuity equations for a Keplerian disk subject to the gravity of the central object and that of embedded protoplanets, and the energy equation in

the case of the adiabatic version. It uses a change of rotating frame on each ring that enables one to increase significantly the time step. The hydrodynamical solver of FARGO resembles the widely known one of the ZEUS code (Stone & Norman 1992), except for the handling of momenta advection. The Coriolis force is treated so as to enforce angular momentum conservation (Kley 1998). The mesh is centered on the primary. It is therefore non-inertial. The frame acceleration is incorporated in the potential indirect term.

#### 5.1.1. Dissipation properties

*Viscosity*— The full viscous stress tensor in cylindrical coordinates of the Navier-Stokes equations, given by Eqs. (12) to (18), is implemented in FARGO. As we shall see by comparing our results to that of the reduced model, which features only the diffusion of load due to the radial shear in Eq. (34), the saturation properties rely essentially on the radial shear, and the other components of the viscous stress tensor appear to be unimportant.

*Diffusivity*— As discussed in section 2.5, we assume that, for our purpose, the evolution of the entropy can be described by a diffusion equation. Since the entropy is not one of the primitive variables handled by the hydrodynamical solver, the thermal diffusion substep updates the internal energy. This substep amounts to solving the following partial differential equation:

$$\partial_t e = e \frac{\kappa}{r} \partial_r (r \partial_r \log s). \quad (64)$$

No diffusion therefore occurs in the unperturbed disk, where  $s$  is a power law of the radius.

#### 5.1.2. Units and common parameters

A number of parameters are common to all the runs that have been performed. These are:

- The planet to star mass ratio is  $q = 10^{-5}$  (this translates into a planetary mass of  $M_p = 3.3 M_\oplus$  if the central star has a solar mass.)
- The disk aspect ratio at the location of the planet is  $h = 0.05$ .
- As our calculations are two dimensional, we have to soften the planetary gravitational potential  $\Phi_p$  over a length scale  $\epsilon$ :

$$\Phi_p = -\frac{GM_p}{\sqrt{r^2 + \epsilon^2}} \quad (65)$$

We performed our calculations with  $\epsilon = 0.5H$ . This value of  $\epsilon$  is meant to give results representative of the dynamics in a slice of the disk at  $|z| \sim 0.5H$ . We note that our results depend indirectly on the value of  $\epsilon$ , since, as we shall see, the degree of saturation of the horseshoe region depends on its half-width  $x_s$ , which is itself a function of the softening length. A systematic study of the dependence of  $x_s$  on the softening length, as well as a study of the corresponding unsaturated torque, has been performed by Masset & Casoli (2009). In section 7.2.1 we add up the contributions from slices at all  $z$  to get a tentative estimate of the three dimensional torque.

<sup>3</sup> <http://fargo.in2p3.fr>

- We strictly remain in the framework either of the barotropic approximation, or in the framework of the study of Masset & Casoli (2009), who assume a flat temperature. In both cases, the initial temperature profile must be flat. In the FARGO code, the temperature profile is imposed through the parameter  $f$  (called flaring index), defined by:

$$h = h_0 \left( \frac{r}{r_0} \right)^f. \quad (66)$$

In a disk with a flat temperature profile, the parameter  $f$  must be set to 1/2.

- In the runs with an energy equation, the adiabatic index  $\gamma$  of the gas is set to 1.4.

### 5.2. Sets of calculations

A general situation involves a disk with arbitrary vortensity and entropy gradients  $\mathcal{V}_g$  and  $\mathcal{S}_g$ , and arbitrary values of viscosity and diffusivity. In this situation, the steady state solution for the entropy, which evolves independently of the load, yields the amount of singular load  $L_g$  that is produced at the downstream separatrices. The general situation therefore amounts to finding a steady state solution  $L$  for the load, that fulfills Eq. (35) and the boundary conditions specified at Eqs. (37) to (39) and (42) with  $L_0 = L_g$  and  $L'_\infty = \mathcal{V}_g/a$ . Owing to the linearity in  $L$  of Eq. (35), we notice that if we have two solutions of this equation  $L_1$  and  $L_2$ , which respectively obey the boundary conditions with  $L'_\infty = \mathcal{V}_g/a$  and  $\Lambda_0 = 0$  for  $L_1$  (hence  $\mathcal{S} = 0$ ), and  $L'_\infty = 0$  and  $\Lambda_0 = L_g$  for  $L_2$ , then  $L_1 + L_2$  is the solution sought for the general problem. The field  $L_1$  corresponds to a barotropic situation (no load is created) with an arbitrary vortensity gradient, while the field  $L_2$  corresponds to a non-barotropic situation with a vanishing vortensity gradient.

This allows us to split the study in two distinct parts:

- A study of the saturation of the vortensity related torque, which we perform on a globally isothermal disk. This study only requires varying the viscosity.
- A study of the saturation of the entropy related torque, in a disk without vortensity gradient. The asymptotic torque value depends on two parameters: the viscosity and the thermal diffusivity.

The torque in a general situation can be deduced by adding the asymptotic values of the torque in these more restricted situations. We nevertheless comment that Masset & Casoli (2009) found a significantly larger width (by up to 10 – 15 %) of the horseshoe region at large value of  $|\mathcal{S}|$ , so that the entropy related torque cannot solely be put on the account of the production of load at the downstream separatrices. This additional complexity may render slightly inaccurate the procedure of adding up the results of the separate cases.

From the above considerations, we performed three series of hydrodynamical calculations: one in a globally isothermal disk, in which we vary the viscosity, and two in a disk with an energy equation, in which we respectively vary the viscosity and the diffusivity. We sum up in Tab. 2 the specific parameters of these series. The

mesh has a radial extent that ranges from  $R_{\min}$  to  $R_{\max}$ , evenly spaced in  $N_{\text{rad}}$  annuli. Azimuthally, it is divided evenly in  $N_{\text{sec}}$  sectors. The calculations were ran for up to either 500 or  $10^3$  orbits, although those which had evidently reached their asymptotic torque value before that date were stopped manually.

We note from Tab. 2 that the isothermal calculations are performed with a flat surface density profile (hence  $\mathcal{V} = +3/2$ ). We do not have any freedom in the choice of the disk parameters for the runs with an energy equation: since those must have  $\mathcal{V} = 0$  and since they must have a flat temperature profile, we find that they have an entropy gradient  $\mathcal{S} \approx 0.43$ . Since this value is positive, we expect a negative entropy related torque.

We also note that the small value of the diffusion coefficients adopted in some of our runs raises the possibility that numerical diffusion due to grid effects could be important. Although we have not undertaken a systematic study of those, we are confident that they are at most of the order of the smallest diffusivity considered here ( $\sim 10^{-9} a^2 \Omega_p$ ). Should that not be the case, numerical diffusion would wash out the torque dependence on viscosity or thermal diffusivity, when either of these quantities is small. As we shall see below, we get a definite, measurable dependence of the torque on the diffusion up the smallest value of the diffusion coefficient (except when the flow becomes chaotic, but even though one can perform time averages and recover a dependence on the diffusion). This clearly indicates that the numerical diffusion present in our runs is negligible.

## 5.3. Results

### 5.3.1. Isothermal runs

The results of set 1 are displayed in Fig. 3. An additional inviscid run is shown, which displays the characteristic sawtooth shape found by Ward (2007) in the framework of the reduced model. Higher viscosity runs converge much before  $t = 500$  orbits, while those with viscosity  $\nu \lesssim 2.10^{-8} a^2 \Omega_p$  still display oscillatory behavior at that date. Evaluating the horseshoe drag from these runs amounts to subtracting the differential Lindblad torque from the total torque. We have noticed that the successive minima and maxima of the horseshoe drag, at very low but non-vanishing viscosity, are in geometric progression, with a common ratio  $r \in ]-1, 0[$ . Differently said, if we denote with  $\gamma_1$  and  $\gamma_3$  the value of two successive minima (maxima) of the total torque and with  $\gamma_2$  the value of the maximum (minimum) in between, then the value of the differential Lindblad torque  $\Delta\Gamma_{LR}$  that we infer assuming that  $(\gamma_i - \Delta\Gamma_{LR})_{i \in \{1,2,3\}}$  are in geometric progression, which is:

$$\Delta\Gamma_{LR} = \frac{\gamma_1\gamma_3 - \gamma_2^2}{\gamma_1 + \gamma_3 - 2\gamma_2}, \quad (67)$$

turns out to be remarkably independent of the set of successive extrema that we consider. This allows us to give a relatively accurate estimate of the differential Lindblad torque, as well as an estimate of the asymptotic value of the torque at low viscosity (which would otherwise require prohibitively long integrations). We find the following value for the differential Lindblad torque:  $\Delta\Gamma_{LR} \approx -2.14\Gamma_0$ . We comment that, in order to evaluate  $\Gamma_0$  by means of Eq. (62), we use a value of  $x_s$  inferred from a

**Table 2**

Parameters used in the different series of calculations. Each series consists of 21 runs, with  $n$  ranging from 0 to 20. The viscosity or diffusivity therefore ranges from  $2 \cdot 10^{-9} a^2 \Omega_p$  to  $2 \cdot 10^{-5} a^2 \Omega_p$ , in a geometric sequence. In the runs with an energy equation, whenever a parameter varies, the other is kept fixed with value  $10^{-6} a^2 \Omega_p$ . This value was chosen to minimize the saturation due to either viscous or diffusive processes.

Name	EOS	$\alpha$	$\nu/(a^2 \Omega_p)$	$\kappa/(a^2 \Omega_p)$	$R_{\min}$	$R_{\max}$	$N_{\text{rad}}$	$N_{\text{sec}}$
S <sub>1</sub>	Isothermal	0	$2 \cdot 10^{-9+n/5}$	—	0.7	1.3	1000	1500
S <sub>2</sub>	Energy equation	3/2	$2 \cdot 10^{-9+n/5}$	$10^{-6}$	0.7	1.4	900	1200
S <sub>3</sub>	Energy equation	3/2	$10^{-6}$	$2 \cdot 10^{-9+n/5}$	0.7	1.4	900	1200

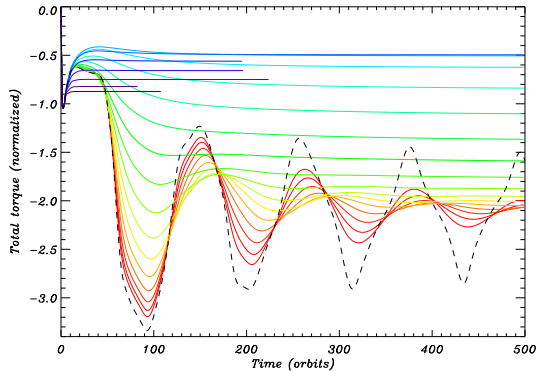


**Figure 3.** Total torque as a function of the time for the runs of set 1 (isothermal equation of state). The dashed line shows an additional inviscid run performed with the same set of parameters than the others. The viscosity ranges from  $2 \cdot 10^{-9} a^2 \Omega_p$  (lower oscillatory curves, darker) to  $2 \cdot 10^{-5} a^2 \Omega_p$  (upper curves, lighter). On the electronic version the viscosity increases as the “wavelength” of the color decreases (the palette is approximately that of the rainbow).

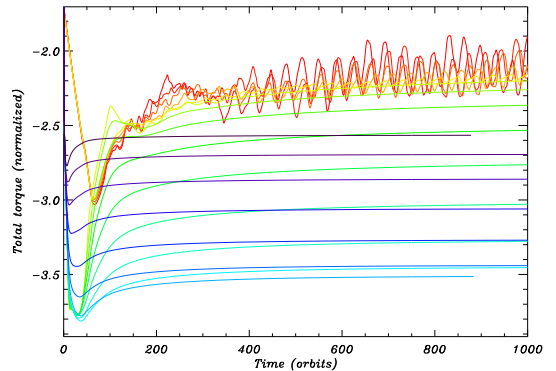


**Figure 4.** Total torque as a function of time for the runs of the set 2 (varying viscosity). The color code is the same as in Fig. 3: a same color refers to the same value of  $n$ . For legibility purposes, the results of runs  $n = 0$  to  $n = 5$  (darker curves, reddish colors on the electronic version) are averaged over a temporal window of width 120 orbits, as they would otherwise display very large oscillations. For larger values of the viscosity a smooth behavior is observed. We note that the time averaging of the torque value distorts its initial behavior: without averaging, the torque of runs  $n = 0$  to 5 would fall on top of the other curves for  $t < 50$  orbits.

streamline analysis. We find  $x_s^{\text{iso}} = 0.0153a$ , a value that is essentially independent of  $\mathcal{V}$  (Masset & Casoli 2009). The corresponding value of  $\Gamma_0$  is used to normalize the torque value in all our isothermal runs.

### 5.3.2. Runs with an energy equation

The results of set 2 and 3 are displayed respectively in Fig. 4 and 5. Calculations performed at low viscosity (therefore in set 2, see Fig. 4) show a highly time varying behavior which prevents from extracting useful average values from these calculations. We shall discuss in a little more detail this behavior in section 6.5.1. It is straightforward to estimate the differential Lindblad torque for these two sets: since there is no vortensity gradient, it suffices to perform a run with the same configuration, but with an isothermal equation of state. The gas being barotropic, the total torque amounts to the differential Lindblad torque, which we divide by  $\gamma = 1.4$  to obtain the differential Lindblad torque in the runs with an energy equation (Baruteau & Masset 2008). We measure  $\Delta\Gamma_{LR} \approx -2.13\Gamma_0$ , where the value of  $x_s$  that we adopt to estimate  $\Gamma_0$  is  $x_s^{\text{iso}}/\gamma^{1/4}$ .

We make the following comment regarding these two sets: in an earlier version of these calculations, we noticed a long term drift of the torque value, which we attributed to a possible issue of boundary conditions associated with a relative drift of the disk’s material with respect to the orbit. In order to get rid of this drift, we have adopted, for these two sets of calculations only, a profile of the

kinematic viscosity that reads:

$$\nu = \nu_0 \left( \frac{r}{a} \right), \quad (68)$$

where  $\nu_0$  is the kinematic viscosity at the orbit. One can check that this prescription yields a vanishing radial drift of the disk’s material for the surface density profile in  $r^{-3/2}$  adopted here. The runs performed with the prescription of Eq. (68) display a better behaved torque on the long term, which allows to measure an asymptotic torque value with a satisfactory accuracy.

We note that the curves at low thermal diffusivity in figure 5 do not pile up at the value of the differential Lindblad torque, which is out of the range of the vertical axis. Although this does not contradict any first principle (since all these runs are performed with the large viscosity  $\nu = 10^{-6} a^2 \Omega_p$ , so that they can sustain an unsaturated corotation torque), this is somehow surprising, as one would expect to be left with a vanishing corotation torque, when the thermal diffusivity tends to zero, since there is no initial vortensity gradient, and since the singular vortensity created at the downstream separatrices tends to zero as the entropy is flattened over the horseshoe region. This is not the case, however, and we will quantify this effect in section 6.4.1.

### 5.4. Comparison with the reduced model

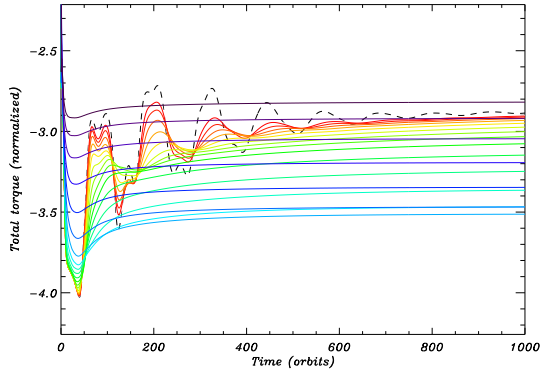


**Figure 5.** Total torque as a function of time for the runs of the set 3 (varying thermal diffusivity). The color code is the same as in Figs. 3 and 4. No temporal averaging is performed for these graphs. The dashed line shows the torque in the adiabatic case (vanishing thermal diffusivity).

We have performed the same set of hydrodynamical calculations presented in section 5.2 in the framework of the reduced model detailed in section 3. We show hereafter how the results of this model compare to the results of the full hydrodynamical calculations. We have chosen  $x_s$  to have the same value as the one we measure for the runs of the full hydrodynamical calculations, using the method of Casoli & Masset (2009), which is  $x_s \approx 0.0153a$ . The mesh of the reduced model has  $N_x = 4000$  and  $N_y = 100$ , and it extends from  $x = -0.3$  to  $x = 0.3$ , as in the hydrodynamical calculations. We add the estimate of the differential Lindblad torque given at section 5.3.1, in order to compare directly the results of full hydrodynamical calculations and those of the reduced model.

We show in Fig. 6 the torque as a function of time in the barotropic case. Apart from the calculations which have a large viscosity, these results compare very well to the full hydrodynamical calculations (Fig. 3), which shows that most of the long term torque behaviour observed in hydrodynamical calculations is accounted for by the horseshoe dynamics and a simple diffusion equation for the load. Even the slow decay of all torques with time, still noticeable at  $t = 500$  orbits, is reproduced in the reduced model. The agreement ceases when the viscosity is too large, namely for  $\nu \gtrsim 2 \cdot 10^6$ . For these values, the timescale of the diffusion of load over the width of the horseshoe region, which is  $\tau_\nu \sim x_s^2/\nu$ , amounts to  $\sim 20$  orbits or less, that is to say, in order of magnitude, the time required to perform a horseshoe U-turn or to establish the horseshoe drag, as can be seen in Fig. 3. For these large values of the viscosity, the vortensity is therefore not conserved during a horseshoe U-turn, a property that is not captured by the reduced model, which assumes that the U-turns are instantaneously performed, so that they strictly conserve vortensity, by virtue of Eqs. (38) and (39).

#### 5.4.1. Cutoff function at large dissipation

The discrepancy at large viscosity underlined above is already noticeable from the results over the first half libration time, i.e. over the first  $\sim 50$  orbits. One should indeed recover the linear estimate of the corotation torque in the limit of large diffusion (Paardekooper & Papaloizou 2008). We first entertain

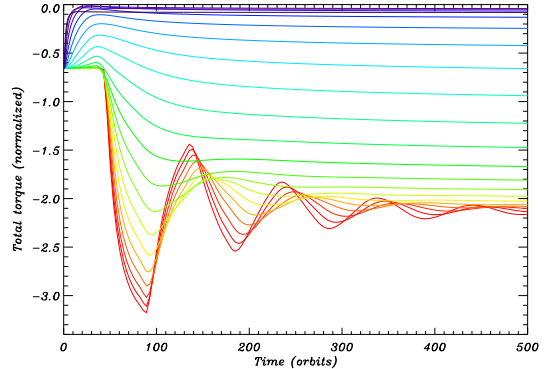


**Figure 6.** Torque as a function of time for the 21 calculations of the run set 1, performed in the framework of the reduced model.

the barotropic case, in the limit of large viscosity.

In order to model in a simple manner this decay, we make the simple assumption that for a given viscosity, the unsaturated corotation torque is a blend of the unsaturated horseshoe drag as given by the reduced model, and of the linear corotation torque, so that:

$$\Gamma_{\text{CR}} = \varepsilon_b \Gamma_{\text{HS}} + (1 - \varepsilon_b) \Gamma_{\text{CR,lin}}, \quad (69)$$

where  $\varepsilon_b \in [0, 1]$  is a blending coefficient. We can extract from our calculations the dependency of the  $\varepsilon_b$  coefficient upon the viscosity, provided we have an estimate of the linear corotation torque. The latter can be estimated by subtracting the differential Lindblad torque from the total torque at  $t \approx 2$  orbits, which yields  $\Gamma_{\text{CR,lin}} \approx 1.0 \Gamma_0$ . We expect that for a sufficiently low viscosity,  $\varepsilon_b \approx 1$ , while  $\varepsilon_b$  should tend to 0 at large viscosity. This suggests the following form for  $\varepsilon_b$ :

$$\varepsilon_b = \frac{1}{1 + K \tau_{\text{U-turn}}/\tau_\nu}, \quad (70)$$

where  $K = O(1)$  is a dimensionless coefficient,  $\tau_{\text{U-turn}}$  is the time scale for a horseshoe U-turn, and  $\tau_\nu = x_s^2/\nu$  is the viscous timescale across the horseshoe region. We measure  $\tau_{\text{U-turn}}$  from the run  $i = 0$  of the set 1, by evaluating the time it takes for a fluid element to go from  $x = x_s, \phi = 1$  rad to  $x = -x_s, \phi = 1$  rad. We find  $\tau_{\text{U-turn}} \approx 1.1 \cdot 10^2 \Omega_p^{-1}$ . We compare the blending coefficient given by the simulations to the trend given by Eq. (70) in Fig. 7. We see in figure 8 how the correction of the reduced model yields results which are in close agreement to those of the full hydrodynamical calculations. From now on, we shall consider that the results of the full hydrodynamical simulations are correctly reproduced by the reduced model to which we apply the cutoff provided by the blending coefficient of Eq. (70). This cutoff can be obtained from short runs, that are limited to the first half libration time after the planet is introduced in the disk.

We repeat a similar analysis for the runs with an energy equation. The decay of the torque at large dissipation can occur either for a large viscosity or a large thermal diffusivity. Assuming the behavior to be separable in viscosity and thermal diffusivity, we find from the analysis of the torque over the first 50 orbits that the following *ad hoc* functions render account of the torque cut off, respectively at large viscosity and at large thermal

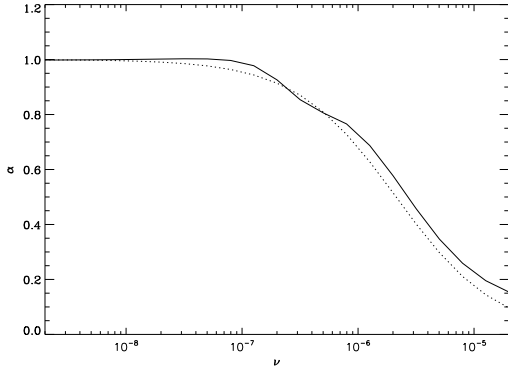


**Figure 7.** Blending coefficient of the isothermal series, as a function of viscosity. The solid curve is extracted from simulations using Eq. (69), whereas the dotted line shows the result of Eq. (70), with  $K = 1$ .

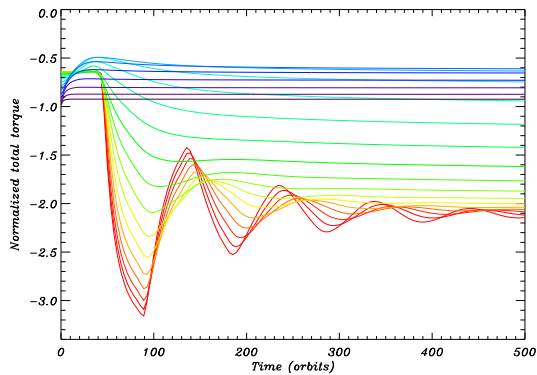


**Figure 8.** Total torque inferred from the reduced model, to which the cutoff of Eq. (70) is applied at large viscosity. This figure should be compared to Fig. 3.

diffusivity:

$$\varepsilon_\nu = \frac{1}{1 + (K\tau_{U-\text{turn}}/\tau_\nu)^2}, \quad \text{with } K = 0.2, \quad (71)$$

$$\varepsilon_\kappa = \frac{1}{1 + K\tau_{U-\text{turn}}/\tau_\kappa}, \quad \text{with } K = 0.5. \quad (72)$$

## 6. SATURATION FUNCTIONS

In this section we work out suitable analytic expressions for the perturbed vortensity and entropy fields at large time, and the corresponding asymptotic horseshoe drag estimates. We perform our analysis in the framework of the assumptions mentioned in section 3.2, together with the boundary conditions specified in section 3.3, and we assume that the flow is steady state in the frame corotating with the planet.

### 6.1. Timescale for the asymptotic regime

In a low diffusion case, it can take a very long time for the vortensity or entropy to relax towards a steady state. For the lowest values considered here ( $\nu = 2.10^{-9}a^2\Omega_P$  or  $\kappa = 2.10^{-9}a^2\Omega_P$ ), the time required to relax towards a steady state over the whole mesh is:

$$\tau_{\text{relax}} \sim \frac{|R_{\text{max,min}} - r_c|^2}{\min(\nu, \kappa)} \sim 10^7 \text{ orbits}. \quad (73)$$

This time, which is longer than the lifetime of the disk if  $a \gtrsim 1$  AU, is much longer than the time scale accessible to fully hydrodynamical calculations, and is still beyond the reach of reduced models (we are able to run reduced models at most over  $\sim 10^5$  orbits). In order to assess the validity of our analytic expressions, we therefore proceed in a two step manner:

- We compare the results of the reduced model with the full hydrodynamical calculations at the final date reached by the latter, in order to assess the accuracy of the results of the reduced model.
- We compare our analytic expressions with the results of the reduced model at much larger times.

### 6.2. Saturation in the barotropic case

We note that Eq. (34), which describes the evolution of the load in the barotropic case, is formally identical to Eq. (36), which describes the evolution of the entropy in the baroclinic case (one has to substitute the load with the entropy, the viscosity with the thermal diffusivity, and the gradient of load with the gradient of entropy). This analysis therefore also provides the information that we shall later need to evaluate the production of load at the downstream separatrix in the baroclinic case, as it requires the value of entropy at the separatrices. For the sake of definiteness, we consider the load in the remaining of this section. Adapting the results to the entropy is straightforward.

#### 6.2.1. Reduction to a convolution equation at low diffusion

If we perform the change of variable  $u \equiv x^{3/2}$ , Eq. (34) can be recast, for  $x > 0$ , as:

$$\frac{8A}{9}\partial_y L = \nu \frac{\partial^2 L}{\partial u^2} + \frac{\nu}{3u} \frac{\partial L}{\partial u}. \quad (74)$$

If we assume that  $L$  varies more rapidly than  $u$ , Eq. (74) can be recast as:

$$\frac{8A}{9}\partial_y L = \nu \frac{\partial^2 L}{\partial u^2}. \quad (75)$$

Eq. (75) is a diffusion equation in which  $y$  plays the role of the time (we note that  $A < 0$ , and that  $y$  decreases as time evolves for a fluid particle with  $x > 0$ ). We denote with  $L_\xi$  the value of the reduced load at  $y = 2\pi a(1 - \xi)$ . We therefore have  $L_0 = L^R$  and  $L_1 = L^F$ . For a given initial configuration  $L_0$  in  $y = 2\pi a$ , the final configuration, after the fluid has executed a full orbit in the corotating frame, is given by:

$$L_1 = L(y = 0) = L_0 \star G, \quad (76)$$

where  $\star$  denotes the convolution product and where the Green's function  $G$  is given by:

$$G(u) = \frac{1}{\pi\sqrt{9\nu a/|A|}} \exp[-u^2|A|/(9\nu\pi a)] \quad (77)$$

The above formulation is valid when the width of the convolution kernel is small compared to the width of the horseshoe region (otherwise edge effects may be important, and a significant diffusion from the region with



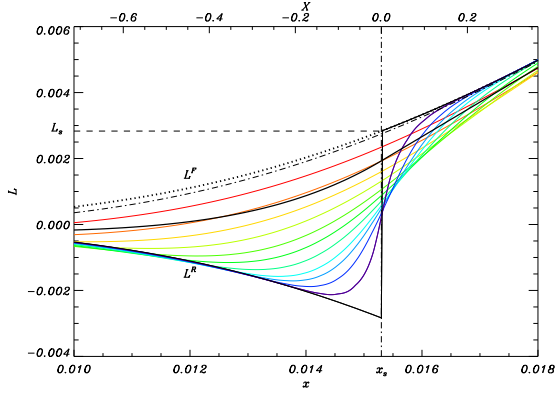


**Figure 9.** Perturbed load for different values of the azimuth. The horseshoe separatrix is at  $x_s = 0.0153$ . The thick solid line, which has a discontinuity in  $x = x_s$  ( $X = 0$ ), represents the field just after the outward horseshoe U-turn (at the rear of the planet). The other curves represent the field value at different values of the azimuth (in geometric sequence). The thick dotted line shows the front load (at  $y = 0$ , just prior to the inward horseshoe U-turn.) It coincides with the rear distribution (solid line) for  $x > x_s$ . The dash-dotted line shows the analytic expectation of Eq. (103). The smooth solid line represents the azimuthal average of the load.

$x < 0$ , which drifts towards increasing values of  $y$ , may occur). This condition translates into:

$$\frac{9\nu a\pi}{|A|} < x_s^3 \quad (78)$$

We define:

$$z_\nu = \frac{a\nu}{\Omega x_s^3}, \quad (79)$$

which represents, within a numerical factor, the ratio of the libration and viscous diffusion time scales across the horseshoe region. The condition of Eq. (78) therefore translates into:

$$z_\nu < 0.026 = z_1^c \quad (80)$$

Similarly we define

$$z_\kappa = \frac{a\kappa}{\Omega x_s^3}, \quad (81)$$

which characterizes the diffusion of entropy. We say that a given value of viscosity (or thermal diffusivity) falls in the regime of low diffusion when Eq. (80) is satisfied (or when  $z_\kappa < 0.026$ ). This means that a localized feature is spread over less than the horseshoe zone width after half a libration time. When this condition is satisfied, we can disregard the shear and write the final distribution of the load, near the separatrix and after a synodic period (half a libration), as a convolution product directly in  $x$ , so that the Green's kernel reads:

$$G(x) = \frac{1}{\sqrt{4\pi\nu\tau_0}} \exp(-x^2/4\nu\tau_0), \quad (82)$$

where  $\tau_0 = 4\pi a/(3\Omega_p x_s)$  is half the horseshoe libration time near the separatrix.

### 6.2.2. Properties of the stationary flow at low diffusion

Figure 9 shows a set of radial cuts of the load for different values of the azimuth, in a regime of low diffusion. One easily checks that this field obeys the boundary conditions given by Eqs. (37), (39), and (44), with  $\Lambda_0 = 0$ : the field represented by the dotted line (front field) is the

opposite of the field represented by the solid thick line (rear field) for  $x < x_s$ , while they coincide for  $x > x_s$ . We focus our analysis on the properties of the field in the vicinity of the separatrix. We aim at providing a universal function that represents the load in normalized coordinates in the low diffusion limit. In steady state, the field verifies the following equalities:

$$L^F = L^R \star G \quad (83)$$

$$L^F(x) = \begin{cases} L^R(x) & \text{if } x > x_s; \\ -L^R(x) & \text{otherwise.} \end{cases} \quad (84)$$

For convenience, we define the variable

$$X = \frac{x - x_s}{\sqrt{4\nu\tau_0}} \quad (85)$$

Eqs. (83) and (84) read, expressed in term of the variable  $X$ :

$$L^F = L^R \star K \quad \text{where } K(X) = \exp(-X^2)/\sqrt{\pi} \quad (86)$$

and

$$L^F(X) = \text{sgn}(X)L^R(X). \quad (87)$$

We consider the function  $f_1$  that verifies Eqs. (86) and (87) and that obeys the following constraints:

$$f_1'(0) = 1 \quad (88)$$

$$\lim_{X \rightarrow -\infty} f_1(X) = 0. \quad (89)$$

This last condition comes from the fact that in the low diffusion limit, the load profile is essentially flattened over the horseshoe region, and therefore tends to zero towards corotation (i.e. for  $X \rightarrow -\infty$ ). This function can be obtained by iteration of the transforms  $T_1$  and  $T_2$  respectively defined by:

$$T_1(f) : X \mapsto \begin{cases} f(X) & \text{if } X > 0 \\ -f(X) & \text{otherwise} \end{cases} \quad (90)$$

and

$$T_2(f) = \frac{f \star K}{(f \star K)'(0)}, \quad (91)$$

where the division of the right hand side is a normalization imposed to ensure that Eq. (88) be satisfied. The action of  $T_1$  represents the U-turns, whereas  $T_2$  describes the viscous diffusion between two subsequent U-turns. We iterate these transforms starting from an arbitrary initial function  $f$ , so that iteration number  $n$  is denoted  $g_n$ :

$$g_n = \underbrace{T_2 \circ T_1 [T_2 \circ T_1 (f)]}_{n \text{ times}}. \quad (92)$$

The iterates are found to converge so that we can adopt  $f_1 = \lim_{n \rightarrow \infty} g_n$ . In this iterating procedure, we set  $g_n$  to 0 below an arbitrary large, negative value of  $X$ , in order to satisfy Eq. (89). It is straightforward to check that the couple of functions  $L^F(X) = f_1(X)$  and  $L^R(X) = \text{sgn}(X)f_1(X)$  thus constructed satisfies Eqs. (86)–(89). The function  $f_1(X)$  is depicted in figure 10. The actual load distribution, and ultimately the horseshoe drag, can be obtained by a proper scaling of the function  $f_1$ . In order to perform this scaling, we need an additional relationship on the radial derivative of the

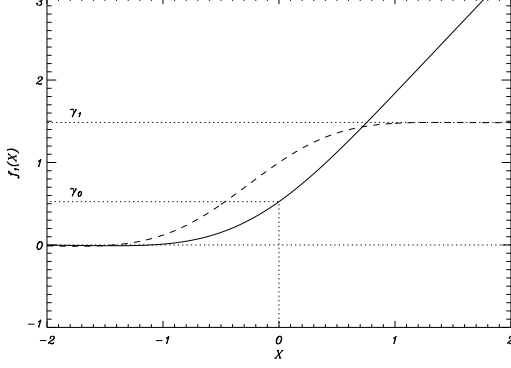


**Figure 10.** Normalized load distribution in the low diffusion limit. The solid line shows  $f_1$ , while the dashed line shows its derivative. The horizontal dotted lines show the value of  $f_1(0)$  and the asymptotic value of  $f'(X)$  for  $X \rightarrow \infty$ .

load. Integrating Eq. (34) in  $y$  over the range  $[0, 2\pi a]$ , and using the boundary condition given in Eq. (37), we note that:

$$\int_0^{2\pi a} L'' dy = 0 \quad \text{for any } |x| > x_s, \quad (93)$$

that is to say the azimuthally averaged slope of the field is uniform outside of the horseshoe region (even though the timescale required to reach this state may be long, as underlined in section 6.1.) Owing to the boundary conditions given at Eqs. (42)–(43), this azimuthally averaged slope is therefore necessarily:

$$\langle L' \rangle = L'_\infty, \quad (94)$$

where the symbol  $\langle \dots \rangle$  denotes the azimuthal average. We can estimate the azimuthally averaged slope of our normalized function in  $X = 0$  (i.e. at the separatrix) in two different, equivalent manners:

- The function  $f_1(X)$  represents the load distribution in front of the planet ( $y = 0$ ). It does not intrinsically contain sufficient information to yield the azimuthally averaged slope. If we note  $\xi = 1 - y/(2\pi a)$  a normalized value of the azimuth (which is 0 at the rear of the planet and 1 in front of the planet), then, in normalized coordinates, the load distribution  $f_\xi(X)$  at azimuth  $\xi$  is given by:

$$f_\xi = T_1(f_1) \star K_\xi = f_0 \star K_\xi, \quad (95)$$

where

$$K_\xi = \frac{1}{\sqrt{\pi\xi}} \exp(-X^2/\xi). \quad (96)$$

The azimuthally averaged slope is then given by:

$$\langle f'_\xi(0) \rangle_\xi = \int_0^1 [T_1(f_1) \star K_\xi]'(0) d\xi \quad (97)$$

We note that when  $\xi \rightarrow 0$ , the slope can be arbitrarily large, and that the function  $f_0 = T_1(f_1)$  is discontinuous in  $X = 0$ , so that a direct estimate of the integral of Eq. (97) may be inaccurate. Rather, if we note  $\gamma_0 = f_1(0) \approx 0.52$ , then we decompose  $f_0$  as follows:

$$f_0(X) = \text{sgn}(X)\gamma_0 + [f_1(X) - \gamma_0]\text{sgn}(X). \quad (98)$$

The first term of the right hand side of Eq. (98) is a step function, whose contribution to Eq. (97) can be evaluated analytically, while the second term of Eq. (98) is continuous in  $X = 0$ , so that an accurate estimate of its contribution can be obtained by direct summation of tabulated estimates of  $[(f_1(X) - \gamma_0)\text{sgn}(X)] \star K_\xi$ . This yields the following estimate of the azimuthally averaged slope, that we denote with  $\gamma_1$ :

$$\gamma_1 = \langle f'_\xi(0) \rangle_\xi \approx 1.48 \quad (99)$$

- One can notice that the slope of the load at any azimuth tends towards a unique value at large  $X$  (and therefore towards the azimuthal average). This can be inferred from examination of Fig. 9, where one can see that the different curves cluster at large, positive values of  $X$ . The asymptotic value of  $f'_1(X)$  at large  $X$  is therefore also  $\gamma_1$ . This is represented in Fig. 10, in which we see directly that  $\gamma_1 \approx 1.48$ .

The load at the upstream separatrix is scaled as follows. It reads:

$$L^F(x) = \mu f_1 \left( \frac{x - x_s}{\sqrt{4\nu\tau_0}} \right), \quad (100)$$

where  $\mu$  is the constant that we aim at estimating. The radial derivative of the load at the separatrix reads, using Eqs. (94) and (99):

$$\partial_x L^F|_{x_s} = \frac{1}{\gamma_1} L'_\infty \quad (101)$$

on the one hand, and, using Eqs. (85) and (88):

$$\partial_x L^F|_{x_s} = \frac{\mu}{\sqrt{4\nu\tau_0}} \quad (102)$$

on the other hand. Using Eqs. (101) and (102) we infer:

$$L^F(x) = \frac{L'_\infty}{\gamma_1} \sqrt{4\nu\tau_0} f_1 \left( \frac{x - x_s}{\sqrt{4\nu\tau_0}} \right). \quad (103)$$

Figure 9 shows this estimates with a dot-dashed line. It compares reasonably well to the true load distribution, which has  $z_\nu \sim 0.014$  in the example shown (half the threshold value of the low diffusion regime). Of particular interest is the value  $L_s$  at the separatrix, upstream of the U-turn. We have:

$$L_s = L^F(x_s) = \mu f_1(0) = L'_\infty \frac{\gamma_0}{\gamma_1} \sqrt{4\nu\tau_0}. \quad (104)$$

Using Eq. (43), Eq. (104) can be transformed using a formal analogy to give the entropy upstream of the horseshoe U-turns, at the separatrices:

$$S_s = S^F(x_s) = S'_\infty \frac{\gamma_0}{\gamma_1} \sqrt{4\kappa\tau_0}. \quad (105)$$

This is a key quantity to evaluate the singular production of load at the downstream separatrices, given by Eq. (48). In the low thermal diffusion regime, the entropy related torque therefore scales with  $\kappa^{1/2}$ .

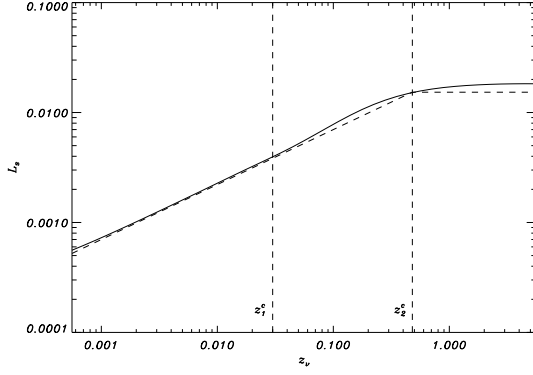


**Figure 11.** Load value on the separatrix, at  $y = 0$ . The dashed line corresponds to Eq. (104) up to values of viscosity that yield the value of the load in the unperturbed disk (i.e. for  $z_\nu < z_\nu^c$ ), and to the value of the unperturbed disk for  $z_\nu > z_\nu^c$ . The solid line corresponds to the results of the reduced model. We see that the analytic expression accurately accounts for the results of the reduced model in the low diffusion regime ( $z_\nu < z_\nu^c$ ). For larger viscosity, some discrepancy is observed, with a maximal relative error of about 20 %.

### 6.2.3. Case of the large diffusion regime

In the low diffusion regime, the value of the load at the upstream separatrix given by Eq. (104) is much smaller than its value in the unperturbed disk, which is

$$L_s^0 = L'_\infty x_s. \quad (106)$$

This is due to the fact that the advection of load within the horseshoe region tends to flatten its profile over the horseshoe region. Reciprocally we expect Eq. (104) to break down when it yields values larger than the unperturbed value, which happens for

$$z_\nu > \frac{3\gamma_1^2}{16\pi\gamma_0^2} \approx 0.48 = z_\nu^c \quad (107)$$

Above this value we expect the diffusion to be sufficiently strong to impose at any instant in time the unperturbed load profile, so we expect the load at the separatrix to saturate at the value  $L_s^0$ . Figure 11 shows how this expectation compares with the results obtained from the reduced model. We see in this figure that the dashed line provides a reasonable approximation to the actual value of the reduced model. We shall adopt henceforth the following approximation of the load value at the separatrix, upstream of the U-turn:

$$L_s = L'_\infty \min\left(x_s, \frac{\gamma_0}{\gamma_1} \sqrt{4\nu\tau_0}\right) \quad (108)$$

for the load in the barotropic case, and

$$S_s = S'_\infty \min\left(x_s, \frac{\gamma_0}{\gamma_1} \sqrt{4\kappa\tau_0}\right) \quad (109)$$

for the entropy value at the separatrix upstream of the U-turn, in the case with an energy equation.

### 6.3. Saturated horseshoe drag

Integrating Eq. (34) from  $y = 0$  to  $y = 2\pi a$  we obtain, in a steady state flow:

$$2Ax[L^R(x) - L^F(x)] = 2\pi a\nu\partial_{x^2}^2\langle L \rangle, \quad (110)$$

which yields for any  $|x| < x_s$ , using Eq. (45):

$$-4AxL^F(x) = 2\pi a\nu\partial_{x^2}^2\langle L \rangle. \quad (111)$$

Integrating by parts, and using the symmetry property of Eq. (44), this allows to transform the horseshoe drag expression of Eq. (59) into:

$$\Gamma = 8\pi B\Sigma_0\nu a^2 [x_s\partial_x\langle L \rangle_s - \langle L_s \rangle], \quad (112)$$

where we have made use of the fact that  $\langle L \rangle_{x=0} = 0$ , which arises from the symmetry property given by Eq. (44). As in Masset (2001), we find that the horseshoe drag reduces to a term to be evaluated at the separatrix. The first term of the bracket of Eq. (112) can be expressed using Eq. (94). The second term requires the estimate of the azimuthal average of the load at the separatrix, much in the same way as we evaluated the azimuthal average of its derivative in section 6.2.2. We obtain:

$$\langle f_\xi(0) \rangle_\xi \approx 0.36 = \gamma_2\gamma_0 \quad \text{with } \gamma_2 \approx 0.68, \quad (113)$$

hence we have, in the low viscosity limit, using Eq. (104):

$$\langle L_s \rangle = \frac{\gamma_2\gamma_0}{\gamma_1} L'_\infty \sqrt{4\nu\tau_0}. \quad (114)$$

Using Eqs. (5), (79), (94), (112) and (114) we can write the horseshoe drag, in the low diffusion limit, as:

$$\Gamma = 8\pi B\nu a \mathcal{V}\Sigma_0 x_s \left[ 1 - \frac{4\gamma_2\gamma_0}{\gamma_1} \left(\frac{\pi}{3}\right)^{1/2} z_\nu^{1/2} \right] \quad (115)$$

$$\approx 2\pi\Omega_p\nu a \mathcal{V}\Sigma_0 x_s (1 - z_\nu^{1/2}), \quad (116)$$

where we have restricted ourselves to the Keplerian case, and where we have used the property:

$$\frac{4\gamma_2\gamma_0}{\gamma_1} \left(\frac{\pi}{3}\right)^{1/2} \approx 0.99 \approx 1. \quad (117)$$

At very low viscosity,  $z_\nu \rightarrow 0$  and  $\Gamma \propto \nu$ . In the low diffusion regime, Eq. (116) can be recast as:

$$\Gamma = \frac{8\pi}{3} \mathcal{V}\Gamma_0 z_\nu (1 - z_\nu^{1/2}), \quad (118)$$

where  $\Gamma_0$  is given by Eq. (62). Figure 12 shows how Eq. (118) compares to the actual horseshoe drag given by the calculations in the framework of the reduced model. This expression is bound to fail at some point since it yields a negative result for  $z_\nu > 1$ . It has a maximum at  $z_\nu = 4/9$ , which is  $(32\pi/81)\mathcal{V}\Gamma_0 \approx 1.24\Gamma_0$ . We see that the agreement between the calculations and this expression is remarkably good up to this value of  $z$  (which roughly coincides with  $z_2^c$ ). Figure 12 shows that beyond  $z_2^c$ , the flat approximation provides a good approximation to the horseshoe drag, with a relative error of about  $\sim 15\%$  at most, for realistic values of the viscosity. We therefore adopt the following expression for the barotropic horseshoe drag:

$$\Gamma = \frac{8\pi}{3} \mathcal{V}\Gamma_0 z_\nu F(z_\nu), \quad (119)$$

where

$$F(X) = \begin{cases} 1 - X^{1/2} & \text{if } X < 4/9 \\ 4/(27X) & \text{otherwise.} \end{cases} \quad (120)$$



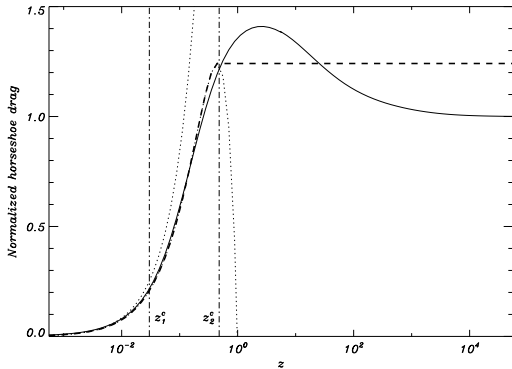


**Figure 12.** Horseshoe drag as a function of viscosity, normalized to  $\mathcal{V}\Gamma_0$ . The solid line shows the results of the reduced models. Note that the viscosity range has been significantly extended towards larger viscosities in order to capture the decay of the horseshoe drag past the peak around  $z_\nu \sim 3$  and its convergence towards the standard unsaturated barotropic horseshoe drag given by Eq. (61). The upper dotted curve shows the linear expression  $(8\pi/3)\mathcal{V}\Gamma_0 z$ , while the lower dotted curve — which coincides with the thick dashed curve for  $z < z_2^c$  — shows Eq. (118). The two vertical dot-dashed lines show the critical values of the viscosity that correspond to  $z_1^c$  and  $z_2^c$ . The thick dashed curve shows Eq. (119)

We note that, in the case of any field that obeys a dynamics similar to that of the load in the barotropic case, i.e. that obeys the governing equation and boundary conditions given at sections 3.2 and 3.3 (without the production of singular stripes at the downstream separatrices), we have the following relationship:

$$x_s \langle \partial_x L \rangle_s - \langle L \rangle_s = x_s L'_\infty F(z_\nu) \quad (121)$$

### 6.3.1. Comparison with hydrodynamical calculations and previous results

We conclude this section with a comparison of the results of hydrodynamical calculations with the analytic expression, and with the expression given by Masset (2001). Figure 13 displays the results of full hydrodynamical calculations at a relatively early stage ( $t = 500$  orbits), as well as the results of the reduced model, at the same date and at a much larger time. Some difference can be noted between these two dates, which shows that the corotation torque at  $t = 500$  has not reached a steady value, in agreement with the slight decay noticeable in the torque curves of figure 3 at large time. The agreement between the full hydrodynamical calculation and the reduced model at the same date is excellent. We note in passing that a slight (10 %) rescaling has been applied to the viscosity value of the reduced model. The saturation state of the horseshoe region depends indeed upon the ratio of the libration timescale to the viscous timescale. This ratio is slightly larger in a real situation than in the corresponding case for the reduced model. Indeed the horseshoe streamlines are not located at a constant distance from corotation. The existence of the potential's indirect term renders the streamline slightly more narrow near opposition ( $\phi = \pi$ ). This effect is more important in thicker disks, and is marginally relevant for the disk aspect ratio of  $h = 0.05$  adopted in our calculations. This has two consequences:

- the libration timescale is slightly larger, as the material drifts slower near the opposition.

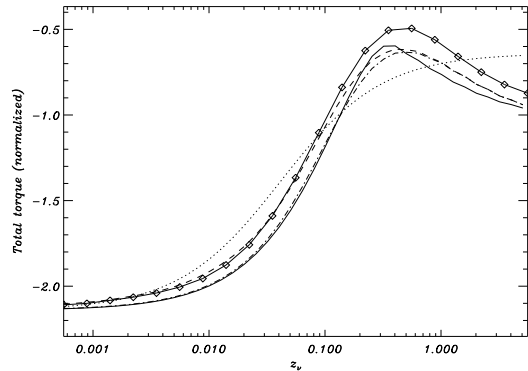


**Figure 13.** Total specific torque as a function of viscosity. The upper solid line with diamonds shows the torque at  $t = 500$  orbits in full hydrodynamical calculations. The dashed and dash-dotted lines show the results of the reduced model, respectively at  $t = 500$  orbits and  $t \sim 10^5$  orbits. The lower solid line shows the analytic expectation given by Eq. (119), while the dotted line shows the analytic prediction of Masset (2001). The torque cutoff function given by Eq. (70) is applied to the reduced model and to the analytic expression, except that of the dotted line.

- the viscous timescale is on the average slightly shorter, as the azimuthally averaged horseshoe width is smaller.

Both effects act at increasing the role of diffusion. A streamline analysis of a typical output of the hydrodynamical calculation shows that the libration to viscous diffusion timescale is  $\sim 1.1$  larger than the crude estimate of the reduced model. Hence the plots of the reduced model results and of the analytical expectations of figure 13 are performed using a value of the viscosity 1.1 times larger than the current viscosity, which amounts to slightly shifting leftward the corresponding graphs on the figure. We make the following additional comments:

- The difference between the analytical expression and the hydrodynamical calculations is entirely accounted for by the date effect: reaching a full steady state is beyond the possibilities of hydrodynamical calculations, and the asymptotic torque is slightly more saturated than at  $t = 500$  orbits.
- The expression of Masset (2001), even if it captures correctly the range of viscosities over which a transition is observed from full saturation to desaturation, does not quite provide as accurate an estimate of the torque value as Eq. (119). This estimate was based upon the simplifying assumption that the material distribution within the horseshoe region has an axisymmetric distribution, which leads to an underestimate of the flow of load on the horseshoe U-turns. In addition, Eq. (119) is much simpler to evaluate than is Eq. (9) of Masset (2001), which involves the evaluation of Airy functions. Since one of the main purposes of the present work is to provide torque expressions that can be used in studies of planetary population synthesis, it is desirable to use an expression which minimizes the computational cost of the torque estimate.

We also notice that the steady state horseshoe drag can be larger than the unsaturated horseshoe drag, given by Eq. (61). This is apparent both for the reduced model

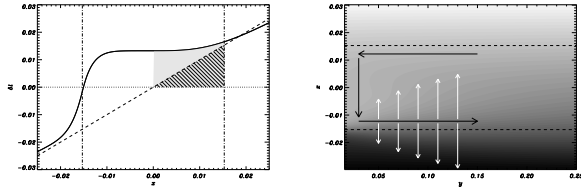


**Figure 14.** Load profile in front of the planet (left) and corresponding map of the load (right). In the left plot, the grey shaded area shows the actual load profile that imposes the horseshoe drag, while the hashed one shows the load profile that corresponds to the standard, unsaturated horseshoe drag given by Eq. (61). In the right plot, the dark arrows sketch the motion of fluid, and the light arrows sketch how viscous diffusion spreads the load out of the horseshoe region (delimited by the dashed line) and to the upstream region.

and for the full hydrodynamical calculations. This behavior can be qualitatively understood as follows: when the viscosity is large, so that the diffusion timescale across the horseshoe region is shorter than the libration timescale, the flow downstream of the U-turns can act back on the upstream flow by diffusion, as sketched on the right plot of figure 14. In a steady state situation, this can result in a load profile in front of the planet significantly above the unperturbed profile, as depicted in the left graph of figure 14. This behavior also yields a value of the load at the separatrix slightly above the unperturbed one, as can be noticed in figure 11. One can estimate the excess of horseshoe drag in the situation depicted in figure 14 by assuming that the load over the upstream part of the horseshoe region (corresponding to the grey shaded area) is uniform and equal to the value that it has at the separatrix in the unperturbed disk. Using Eq. (59), it is straightforward to see that the horseshoe drag then supersedes the standard value by a factor  $4/3$ . This is in good agreement with the peak value of the horseshoe drag in figure 12. We comment that this excess is less pronounced in full hydrodynamical calculations, since it corresponds to values of the viscosity for which some cutoff already occurs.

#### 6.4. Saturation of the entropy related torque

We examine in this section the saturation properties of the entropy related torque, and exhibit an analytic expression for the steady state entropy related corotation torque. Describing the saturation properties of the entropy related torque amounts to finding the steady state pattern of load that settles over a long time scale, when it receives a singular kick described by Eqs. (38) and (39) at each horseshoe U-turn, much as in the barotropic case. As explained in section 5.2, we split the general case into a bulk term that has a non-vanishing slope at infinity, and an edge term that has a flat profile at infinity but undergoes the creation of singularities at the downstream separatrices. We focus firstly on the bulk term, and we disregard the singularities.

##### 6.4.1. Vortensity-Entropy viscous coupling

For a barotropic disk we have made the simplifying assumption that the load (or vortensity) evolution could be described by a diffusion equation, i.e. we have neglected the last term of Eq. (25), so that the evolution equation of the load was described by Eq. (26). Nevertheless, the last term of Eq. (25) may be arbitrarily large at a contact discontinuity, and we may expect this term to play

a significant role in runs with an energy equation, at low diffusivity, when the contact discontinuity does not significantly decay along the separatrices. Under these circumstances, the contact discontinuity may act as a source of load, which ultimately exerts a corotation torque. In order to work out the contribution to the torque of the load thus created, we make two amendments to the calculations developed in the previous section: (i) the coupled evolution of the load and of the entropy is different, and described by the evolution of an eigenfunction that is a linear combination of load and entropy; (ii) the integration by parts presented in section 6.3 must be modified accordingly, and yields a torque expression different from that of Eq. (112). We briefly describe hereafter the corresponding calculations.

The evolution of the system, which is governed by Eq. (35) and Eq. (36), can also be described using the eigenfunction  $U$  defined by:

$$U = L - \frac{2\nu}{\gamma(\nu - \kappa)} S. \quad (122)$$

By virtue of the radial boundary conditions of Eqs. (42) and (43), the asymptotic slope of  $U$  at large  $|x|$  is given by:

$$\lim_{x \rightarrow \pm\infty} \partial_x U \equiv U'_\infty = \frac{\mathcal{V}}{a} - \frac{2\nu}{\nu - \kappa} \frac{\mathcal{S}}{a}. \quad (123)$$

The governing equations of  $U$  are therefore similar to those of  $L$  in the barotropic case, except that  $U$  has a different slope at infinity. Namely, the evolution of the system is described by:

$$\partial_t U + 2Ax\partial_y U = \nu U'', \quad (124)$$

together with Eq. (36) and the boundary conditions of Eqs. (123) and (43). Also the function  $U$  undergoes the creation of singularities  $\pm L_0$  at the downstream separatrices, as described in Eqs. (38) and (39), since  $L$  has a unitary weight in Eq. (122). As explained above, we disregard these singularities in this section, and we focus on the bulk term exclusively. The contribution of the singular creation of load will be analyzed in the next section.

We integrate Eq. (35) from  $y = 0$  to  $y = 2\pi a$ , assuming a steady state. This yields:

$$-4AxL^F = 2\pi a\nu \langle L'' \rangle - \frac{4\pi a\nu}{\gamma} \langle S'' \rangle. \quad (125)$$

We multiply Eq. (125) by  $8B^2ax$ , and integrate it by parts between 0 and  $x_s$ :

$$\Gamma_{\text{HS}} = 8\pi B a^2 \nu \Sigma_0 \left[ x_s \langle U'_s \rangle - \langle U_s \rangle + \frac{2}{\gamma} \frac{\kappa}{\nu - \kappa} (x_s \langle S'_s \rangle - \langle S_s \rangle) \right] \quad (126)$$

Using Eq. (121), which applies to a field such as  $U$ , as we outlined in section 6.3, we write:

$$x_s \langle U'_s \rangle - \langle U_s \rangle = U'_\infty x_s F(z_\nu) \quad (127)$$

and

$$x_s \langle S'_s \rangle - \langle S_s \rangle = S'_\infty x_s F(z_\kappa). \quad (128)$$

Using Eqs. (62), (123), (126), (127) and (128) we write:

$$\Gamma_{\text{HS}} = \frac{8\pi}{3}\Gamma_0 z_\nu \left[ \mathcal{V}F(z_\nu) - 2\mathcal{S} \left( \frac{z_\nu F(z_\nu) - z_\kappa F(z_\kappa)}{z_\nu - z_\kappa} \right) \right]. \quad (129)$$

The last term in the bracket of Eq. (129) represents the additional contribution due to the vortensity-entropy viscous coupling in Eq. (36). By continuity, in the particular case  $\nu = \kappa$  (unitary Prandtl number), the torque is:

$$\Gamma_{\text{HS}} = \frac{8\pi}{3}\Gamma_0 z_\nu [\mathcal{V}F(z_\nu) - 2\mathcal{S}\partial_{z_\nu}[z_\nu F(z_\nu)]] \quad (130)$$

Eq. (130) constitutes the bulk horseshoe drag in the general case. This bulk term renders account accurately of the corotation torque that we obtain at low thermal diffusion and finite viscosity (runs set 3, see section 5.3.2). In this situation, the entropy gradient virtually vanishes across the horseshoe region, so the corotation torque essentially reduces to the bulk term, which reads, in this particular situation with  $z_\kappa/z_\nu \rightarrow 0$  and  $\mathcal{V} = 0$ :

$$\Gamma_{\text{HS}} = \frac{8\pi}{3}\Gamma_0 (-2\mathcal{S})F(z_\nu). \quad (131)$$

The torque is therefore  $-2\mathcal{S}/\mathcal{V}$  times that of the barotropic situation with  $\nu = 10^{-6}a^2\Omega_p$ , which is what one can infer from the Figs. 3 to 5.

We now turn to the edge term which stems from the vortensity sheets at the downstream separatrices. We comment that in order to isolate its effect in numerical simulations, it was necessary to firstly establish Eq. (130) so as to subtract it from the horseshoe drag, since, in general, Eq. (130) shows that there is always a bulk term associated to the edge term (i.e. when there is a non-vanishing entropy gradient), even in disks with a flat vortensity profile.

### 6.5. Corotation torque associated to the singular production of load

As we have already considered in the previous section the bulk term in the general case, which stems from a non-vanishing large scale slope of  $U$ , we now consider the complementary situation and isolate the effects of the singular production of load at the downstream separatrices, and assume a vanishing large scale slope:  $U'_\infty = 0$ . Owing to the linearity of the flow governing equations, the total torque is the sum of both contributions.

#### 6.5.1. Considerations about the inviscid case

The special case of an inviscid disk deserves some discussion. It has already been noted in numerical simulations that in inviscid disks with thermal diffusion, the corotation torque tends to zero after several libration timescales, so that some viscosity is needed to prevent saturation (Baruteau 2008; Paardekooper & Papaloizou 2008; Kley & Crida 2008). This is expected on general grounds, as a sustained exchange of angular momentum between the horseshoe region and the rest of the disk, described by the Navier Stokes equations, necessarily relies on a non-vanishing stress tensor, regardless of the thermal diffusivity (Masset & Casoli 2009; Masset 2008a,b). This simple remark provides a strong clue about the origin of the entropy related torque. It had been initially argued that this component of the horseshoe drag came

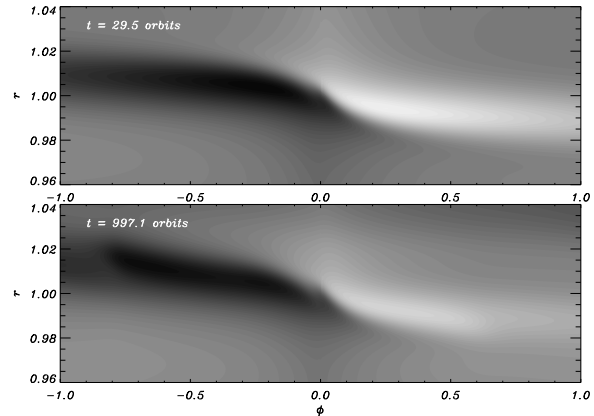


**Figure 15.** Perturbed entropy in a nearly inviscid disk with thermal diffusion. The grey level is the same for both plots. The upper plot corresponds to a situation during the first half libration time, i.e. to the fully unsaturated horseshoe drag, while the lower plot corresponds to approximately 12 full libration times.

from the under- and over-dense regions that appear at the ends of the horseshoe region as the result of material conserving its entropy whereas the pressure remains essentially unchanged (Paardekooper & Papaloizou 2008; Baruteau & Masset 2008). More recently, it has been argued that this effect does not contribute to the entropy related torque, which exclusively arises from the singular production of load at the downstream separatrices (Masset & Casoli 2009). Figure 15 illustrates why this has to be the case indeed. It shows maps of perturbed entropy corresponding to the run of set 2 with viscosity  $\nu = 2 \cdot 10^{-9}a^2\Omega_p$  (so that it can be considered, for our purpose, as an inviscid run). The thermal diffusivity in all the runs of this set is such that the thermal diffusion time is longer than the horseshoe U-turn time (so that material performing the U-turns behaves adiabatically) but slightly shorter than half the libration timescale, so that a fixed pattern of perturbed entropy subsists forever in the horseshoe region (associated with a corresponding pattern of perturbed density). Nevertheless, the corotation torque tends to zero (on the average, since the situation is very messy owing to the presence of vortices), as it has been seen in figure 4. This rules out the possibility that this localized pattern contributes, even partially, to the entropy related torque, as was recently suggested by Paardekooper et al. (2009). If it did, the corotation torque could not possibly saturate at null viscosity and finite thermal diffusion, which is in contradiction with first principles. With this in mind, it is instructive to undertake a simple minded analysis of the inviscid case. We consider a planet “switched on” in a initially unperturbed disk without vortensity gradient. A singular amount of load  $\pm\Lambda_0$  begins to drift along the downstream separatrices. After a time  $\tau_0$ , the singular load has executed a complete orbit in the corotating frame. We can consider that the singular amount of load has spread radially as a vanishingly narrow Gaussian under the action of a vanishingly small viscosity. In an idealized situation, the half part of the Gaussian packet that is outside of the horseshoe region circulates in the outer (inner) disk, whereas the other half is shunt on a horseshoe U-turn. In practice, however, the horseshoe region is not strictly closed, especially at early times, and can have a slightly different width in front of the planet and behind it (Casoli & Masset 2009). We there-

fore entertain a slightly more general situation in which a fraction  $1/2 - \chi$  of the singular load circulates, whereas the remaining fraction  $1/2 + \chi$  is shunt toward horseshoe U-turns, as depicted in figure 16. We denote  $\Lambda_n$  the load at the front separatrix, downstream of the U-turn, over the time interval  $[n\tau_0, (n+1)\tau_0[$ . The load value at this location changes every  $\tau_0$ , and so does the torque by virtue of Eq. (59). Figure 16 shows the relationship between  $\Lambda_{n-1}$  and  $\Lambda_n$ :

$$\Lambda_n = \left(\frac{1}{2} - \chi\right) \Lambda_{n-1} - \left(\frac{1}{2} + \chi\right) \Lambda_{n-1} + \Lambda_0 = -2\chi\Lambda_{n-1} + \Lambda_0. \quad (132)$$

From this recurrence relation we infer:

$$\Lambda_n = \begin{cases} \frac{\Lambda_0}{1+2\chi} [1 - (-2\chi)^{n+1}] & \text{if } \chi \neq -1/2 \\ (n+1)\Lambda_0 & \text{if } \chi = -1/2, \end{cases} \quad (133)$$

and the corresponding torque value is, using Eqs. (59) and (133):

$$\Gamma_n = 16|A|B^2ax_s^2\Lambda_0(-2\chi)^n. \quad (134)$$

In the general case ( $|\chi| < 1/2$ ), the torque tends to zero at large time. It does so after just half a libration time in the particular case  $\chi = 0$ . If  $\chi > 0$ , it oscillates about 0, whereas it tends monotonically to 0 if  $\chi < 0$ . The ideal situation ( $\chi = 0$ , i.e. the load is equally split at the stagnation point between circulation and horseshoe U-turn) is more likely to be found in a ‘‘quiet’’ situation, for instance at large softening length. We expect in that case that the torque quickly saturates (note that in practice, the value of  $\Lambda_0$  changes over time until the entropy field reaches a steady state, so that the thermal diffusion timescale determines the minimum amount of time needed to reach the torque saturation).

The peculiar cases  $|\chi| = 1/2$  are also of interest.

- If  $\chi = 1/2$  (which means that the whole amount of load executes horseshoe U-turns), the torque indefinitely oscillates about 0. The field does not converge towards a steady state. However, the time averaged torque does converge to zero, which can be considered as a weak version of the torque saturation.
- If  $\chi = -1/2$  (which means that the load produced at the stagnation point never undergoes horseshoe U-turns), the load increases (decreases) steadily at the inner (outer separatrix). This rather artificial case therefore corresponds to a steady flow of material from one side of the horseshoe region to the other side, which gives rise to a non vanishing corotation torque, much as in type III migration (Masset & Papaloizou 2003).

Therefore, apart from the artificial case  $\chi = -1/2$ , the torque is bound to saturate. The manner in which it does so depends on the value of  $\chi$ , hence it depends on very local properties of the flow in the vicinity of the stagnation point. It can either oscillate significantly before saturating, or it can tend to zero quickly and monotonically. This simple minded analysis therefore illustrates the fact that, even if the asymptotic value does not depend on the details of the flow, the manner in which the torque saturates is highly sensitive to the flow topology,

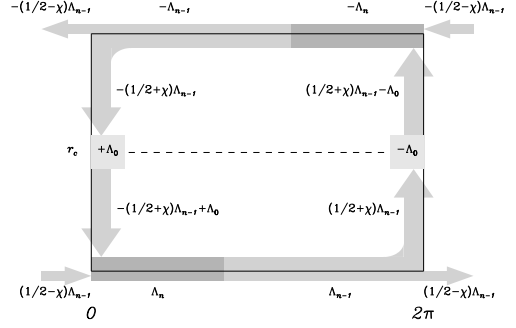


**Figure 16.** Sketch of the load at a given instant in time in an inviscid disk. The  $x$ -axis is the azimuth and the  $y$ -axis is the radius. The horizontal solid lines show the separatrices, while the dashed line shows the corotation.

and it may differ from one particular case to the other. This is quite in contrast with the behavior of the bulk term, in which the torque value is dominated by phase mixing, and has a temporal behavior much more robust and predictable.

#### 6.5.2. Universal form of the load in the low viscosity limit

We seek the steady state distribution of the load in the low diffusion limit. This amounts to finding a distribution which has a vanishing slope for  $|X| \rightarrow \infty$  and which satisfies Eq. (83) and the following relationship:

$$L^R(x) = -L_0\delta(x - x_s) + \begin{cases} L^F(x) & \text{if } |x| > x_s; \\ -L^F(x) & \text{otherwise.} \end{cases} \quad (135)$$

Using the variable change of Eq. (85), we can recast these conditions as Eq. (86) and:

$$L^R(X) = \text{sgn}(X)L^F(X) + \xi\delta(X), \quad (136)$$

where  $\xi = -L_0/\Delta$ . We seek a couple of functions ( $L^F, L^R$ ) that verifies Eqs. (86) and (136) with  $\xi = 1$ . It is straightforward to check that if one adopts for  $L^F(X)$  the function  $g_1(X)$  defined by  $g_1(X) = f'_1(X)/(2\gamma_0)$ , where  $f_1$  is the function that has been obtained in section 6.2.2, and for  $L^R(X)$  the function given by Eq. (136), then the functions  $L^F$  and  $L^R$  so constructed verify Eq. (86). The function  $f'_1(X)$  is represented in Fig. 10.

For an arbitrary value of  $L_0$ , we have therefore:

$$L^F(X) = \xi g_1(X) = -\frac{L_0}{\Delta} g_1(X). \quad (137)$$

The horseshoe drag of Eq. (59) can be written

$$\Gamma_{\text{HS}} = 2 \int_0^{x_s} x^2 L(x) dx + L_0 x_s^2, \quad (138)$$

which we expand, to first order in  $\sqrt{4\nu\tau_0}/x_s$ , as

$$\frac{\Gamma_{\text{HS}}}{8|A|B\Sigma_0 a} = L_0 x_s^2 + 2x_s^2 \int_{-\infty}^0 L^F(X) dX - 4\Delta L_0 x_s \int_{-\infty}^0 X g_1(X) dX, \quad (139)$$

A property of  $g_1(X)$  is that:

$$\int_{-\infty}^0 g_1(X) dX = f_1(0)/(2\gamma_0) = 1/2, \quad (140)$$

so that the horseshoe drag expression above reduces to:

$$\Gamma_{\text{HS}} = -32|A|B\Sigma_0 a \sqrt{4\nu\tau_0} L_0 x_s \int_{-\infty}^0 X g_1(X) dX. \quad (141)$$

The integral on the right hand side of Eq. (141) is approximately equal to  $-0.176$ , hence we can reduce the torque expression to, using Eq. (47):

$$\Gamma \approx 2.82 \sqrt{\frac{\pi}{3}} z_\nu^{1/2} \Gamma_1. \quad (142)$$

The above expression, when compared to the results of the reduced model (not reproduced here), correctly accounts for a  $\nu^{1/2}$  dependence, but overestimates the horseshoe drag of the reduced model by a significant factor (about 1.6). The reason for this can be tracked back to the simplification of Eq. (139) arising from Eq. (140), and it illustrates again the high sensitivity of the torque edge term to the detail of the processes that affect the load advected along the separatrix. Whereas Eq. (140) is exact in the framework of the set of Eqs. (136) and (86), which come themselves from Eq. (75), it is only approximate when the shear is retained, which means that a singular amount of load drifting along the separatrix is not exactly split into two equal fractions on the inside and on the outside of the separatrix. It is straightforward to estimate the magnitude of this effect. We define the true load  $L_t(X)$  distribution as the approximate one determined above plus a residue  $\delta L(X)$  that we want to characterize:

$$L_t(X) = L(X) + \delta L(X), \quad (143)$$

and we make the assumption that  $|\delta L| \ll |L|$ . If we inject this into Eq. (74), we obtain, after integrating from  $y = 0$  to  $y = 2\pi a$ :

$$\frac{16}{3}|A|\delta L^F = 2\pi a \frac{\nu}{u} \partial_u \langle L \rangle. \quad (144)$$

The horseshoe drag of Eq. (139) then becomes:

$$\frac{\Gamma_{\text{HS}}}{8|A|B\Sigma_0 a} = 2x_s^2 \int_{-\infty}^0 \delta L^F(X) dX - 4\Delta L_0 x_s \int_{-\infty}^0 X g_1(X) dX. \quad (145)$$

In the low diffusion regime, the first integral of the right hand side of Eq. (145) reduces to:

$$\int_0^{x_s} \delta L^F(X) dX = \frac{\pi a \nu}{4|A|x_s^2} \langle L \rangle_s. \quad (146)$$

Using the relationship  $\langle L \rangle_s = \gamma_1 L^F$ , we end up with an estimate of the additional contribution to the horseshoe drag due to  $\delta L$  (the first term of the right hand side of Eq. (145)):

$$\delta \Gamma_{\text{HS}} = 16|A|B\Sigma_0 a x_s^2 \int_0^{x_s} \delta L^F(X) dX \quad (147)$$

$$= -\frac{\gamma_1}{4\gamma_0} \sqrt{\frac{\pi}{3}} z_\nu^{1/2} \Gamma_1. \quad (148)$$

Adding up Eqs. (142) and (148), we eventually get

$$\Gamma_{\text{HS}} \approx 2.11 \sqrt{\frac{\pi}{3}} z_\nu^{1/2} \Gamma_1 \approx 2.16 z_\nu^{1/2} \Gamma_1, \quad (149)$$

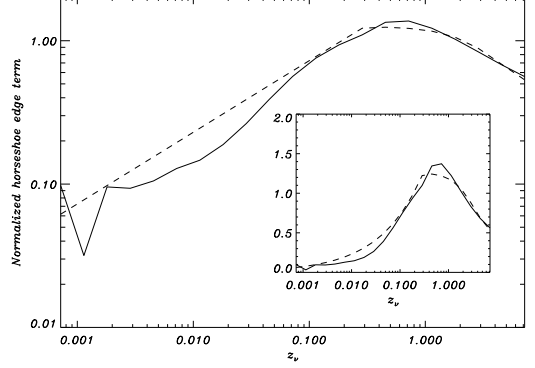


**Figure 17.** Entropy related torque (edge term), as a function of viscosity. The solid line shows the value inferred from the runs of set 2 (to which the estimated bulk horseshoe drag given by Eq. (129) has been subtracted), while the dashed line shows the results of Eqs. (150)–(151). The value chosen for  $\Gamma_{CR,lin}$  is  $\Gamma_1/3$ , given by estimates of the torque value only 2 orbits after the insertion of the planet in the disk. The inset plot represents the same quantity with a linear scale on the  $y$ -axis.

which agrees with the results of the reduced model within 20 %.

### 6.5.3. Extension to arbitrary viscosity

Eq. (149) remains valid as long as the viscosity is sufficiently small. Results obtained in the framework of the reduced model (not reproduced here) show essentially two branches: the branch in  $\nu^{1/2}$ , corresponding to the regime of low viscosity, and a flat branch at large viscosity. These two branches intersect at  $z_\nu = 0.3$ , hence we adopt the following expression for the horseshoe drag edge term:

$$\Gamma = \Gamma_2 \varepsilon_\nu + \Gamma_{CR,lin} (1 - \varepsilon_\nu), \quad (150)$$

where

$$\Gamma_2 = 2.16 \sqrt{\min(z_\nu, 0.3)} \Gamma_1 \quad (151)$$

represents the analytic trend derived in the previous section, saturated at  $z_\nu = 0.3$ , and where  $\varepsilon_\nu$ , given by Eq. (71), is meant to represent the decay towards the linear torque at large viscosity. We note that Eq. (151) implies, in agreement with the results of the reduced model, an overshoot of the edge term of about 20 %, much as the one we noticed in the barotropic case (see section 6.3.1).

We note that so far we have assumed that the vortensity sheet produced at the downstream separatrices has the same value as in the unsaturated case. Actually, the horseshoe dynamics acts on the entropy in exactly the same way as it does with the vortensity in the barotropic case, so that the entropy jump at the stagnation point can be lower than in the unsaturated case. It is the purpose of the following section to check the dependence of the entropy jump (and therefore of the torque) on the diffusivity. Here, in order to assess the correctness of Eq. (150) in our full hydrodynamical runs, we simply measure the entropy difference upstream of the U-turns, in the saturated state. This difference is the same for all runs of set 2, and turns out to be 0.7 times the difference in the unperturbed disk.

Figure 17 shows that there is an overall correct agreement between the results of Eq. (150)–(151), and the results of numerical simulations. We mention at very

low viscosity, the situation is very messy owing to the presence of vortices, as described in section 5.3.2, and the range of our time average (500 orbits) is too short to exhibit a neat trend. We also comment that over the first decade of viscosities, the viscous time across the horseshoe region is larger than the duration of the runs, so that the corresponding runs have not necessarily reached their asymptotic value.

#### 6.5.4. Dependence on diffusivity

We now examine how the horseshoe drag edge term depends on thermal diffusion. We consider that the dependencies of this term on viscosity and on diffusivity are separable: its asymptotic value is the product of a function of  $z_\nu$  exclusively (which we analyzed at the previous section) by the load produced downstream of the horseshoe U-turns (which depends on the diffusivity exclusively, as the latter determines the entropy jump that subsists upstream of the U-turns). We have checked this assumption with an additional set of lower resolution runs, not reproduced here, with diffusivity  $\kappa = 3 \cdot 10^{-7} a^2 \Omega_p$ .

We firstly note that the value of the viscosity chosen in set 3 ( $\nu = 10^{-6} a^2 \Omega_p$ ) corresponds nearly to the peak value in Fig. 17, so that we make the simplifying assumption that the horseshoe drag measured in these runs corresponds to the unsaturated horseshoe drag with a lower load creation at the downstream separatrices due to a lower entropy jump. This yields to the torque expression:

$$\Gamma = \Gamma_1 \frac{S_s}{S'_\infty x_s}, \quad (152)$$

where  $\Gamma_1$  is the unsaturated horseshoe drag edge term (see e.g. Eq. (96) of Masset & Casoli 2009), and where  $S_s$ , the entropy value at the separatrix upstream of the U-turn, is given by Eq. (109). Taking into account the cut-off at large diffusivity, Eq. (152) eventually yields:

$$\Gamma \approx \Gamma_1 \min \left( 1, 4 \sqrt{\frac{\pi}{3}} \frac{\gamma_0}{\gamma_1} z_\kappa^{1/2} \right) \varepsilon_\kappa \approx \Gamma_1 \min(1, 1.4 z_\kappa^{1/2}) \varepsilon_\kappa. \quad (153)$$

We note that we do not add a blend of the linear torque value at large diffusivity, counter to what we have done in the analysis of dependence upon viscosity. Although we expect to recover the linear torque value at large viscosity, we expect the disk to behave isothermally in the limit of large diffusivity. Since there is neither a vortensity gradient nor a temperature gradient in the disk, we expect the corotation torque to vanish in this limit.

Figure 18 shows that there is an overall correct agreement between Eq. (153) and the results of simulations. We note that the entropy at very low diffusivity has not settled yet to the expected value, as the thermal diffusion timescale is longer than the duration of the simulations. We also mention that, whereas the correction due to the bulk term, given by Eq. (130), was a minute effect in the previous section, it is a significant effect here, in particular at low thermal diffusion where a significant viscous creation of load occurs along the separatrices and gives rise to a relatively strong bulk term, as already pointed out in sections 5.3.2 and 6.4.1.

## 7. SIDE RESULTS AND ADDITIONAL COMMENTS

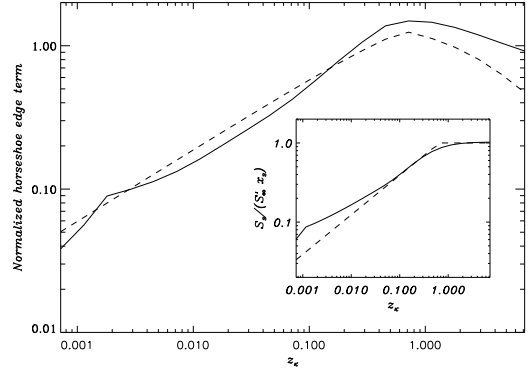


**Figure 18.** Entropy related torque (edge term) as a function of diffusivity. The solid line shows the value given by the simulations, corrected from the bulk term of Eq. (129), while the dotted line indicates the prediction of Eq. (153). The inset plot shows the ratio of the viscosity difference upstream of the U-turns to this difference in an unperturbed disk (solid line) compared to the expression of Eq. (109) (dashed line). The torque values correspond to time averages from 800 to 1000 orbits, while the entropy jump is measured at  $r = a \pm x_s$ ,  $\phi = \pm 1$  rad, on a time average of the entropy field between 700 and 1000 orbits.

Prior to the full torque expression, which will be given in section 8, we briefly present additional results obtained from a systematic study of the differential Lindblad torque, and we lay down the set of assumptions used to provide the final torque expression provided in section 8.

### 7.1. Diffusivity dependence of the differential Lindblad torque

For the sake of completeness, we have undertaken an additional study of the Lindblad torque dependence on the diffusivity. At low diffusivity, the acoustic waves that constitute the wake essentially behave as adiabatic waves, whereas at large diffusivity, they behave isothermally. Since the differential Lindblad torque scales as  $c_s^{-2}$ , where  $c_s$  is the sound speed, one should recover a differential Lindblad torque value  $\gamma$  times larger in the isothermal limit than in the adiabatic limit. We have therefore run calculations in which we have a vanishing vortensity gradient and a vanishing entropy gradient (which implies  $\alpha = 3/2$  and  $f = 1/5$ ) so as to have a vanishing corotation torque. These calculations are run over a short time interval (typically 10 orbits), which is sufficient for the Lindblad torque to reach a steady state value (Meyer-Vernet & Sicardy 1987). We comment that we modified the diffusivity procedure for these specific calculations, as we had initially linked the amount of thermal diffusion to the Laplacian of the entropy, in order to filter out a possible dependence of the Lindblad torque on the diffusivity (see section 2.5). In the present case we use the standard dependency upon the Laplacian of the temperature. In the case of a single acoustic wave in a uniform medium at rest, the transition of the phase velocity from  $c_s$  to  $\gamma^{1/2} c_s$  depends on the dimensionless parameter  $\rho = c_s^2 / (\omega \kappa)$ , where  $\omega$  is the wave frequency. This parameter represents the ratio of the wave period to the diffusion timescale across one wavelength. We therefore expect the transition of the Lindblad torque to occur for a critical value of the diffusivity that is

$$\kappa_c = a^2 \Omega_p h^2, \quad (154)$$

obtained by letting  $\rho = 1$  and adopting  $\omega = \Omega_p$  for the frequency of the waves seen in the matter frame, since those are excited at their Lindblad resonances (where the wave frequency matches the epicyclic frequency, hence the orbital frequency in a Keplerian disk). We note that the characteristic length scale in the wake excitation region is  $H$ , which is also the largest scale of turbulence, so that the diffusion approximation should be on the edge of its domain of validity, much as for the horseshoe drag, as was discussed in section 2.1. This critical value of the diffusivity is much larger (by two orders of magnitude) than the maximum diffusivity considered in our exploratory analysis of the corotation torque. In the Lindblad torque runs, we find that indeed the Lindblad torque has a value that is roughly the mean of the isothermal and adiabatic limits for this value of the diffusivity, and we provide the following fit to the dependency that we have obtained:

$$\frac{\Gamma_{LR}}{\Gamma_{LR}^{iso}} \approx f(\kappa/\kappa_c, \gamma), \quad (155)$$

where  $f(x, \gamma)$  is defined by:

$$f(x, \gamma) = \frac{(x/2)^{1/2} + 1/\gamma}{(x/2)^{1/2} + 1} \quad (156)$$

## 7.2. Assumptions for the torque expression

### 7.2.1. Transition from two dimensions to three dimensions

The study that we have presented in this paper is two dimensional, for reasons of computational cost, so that the final torque expression is smoothing dependent. Useful torque expressions should however be three-dimensional, so that we scale our torque value by the three-dimensional estimates given by Masset & Casoli (2009). These estimates were obtained by assuming horizontally layered motion in the coorbital region, and by integrating the contribution of all slices, assumed to be given, by virtue of Pythagoras' theorem, by two dimensional estimates in which the smoothing length is the layer's altitude. This approach, albeit not genuinely three dimensional, is more sophisticated than a two dimensional study with a fixed, reasonable value adopted for the smoothing length.

We note that the saturation of the corotation torque depends on the ratio of the libration timescale to the diffusion time scale (be it the thermal or viscous diffusion timescale). This ratio depends on the altitude in the disk, and its estimate requires an estimate of the width of the horseshoe region at each altitude. Since most of the torque arises from the layers which are located near the equatorial plane of the disk, we simply assume that the saturation function of the three dimensional torque can be correctly described by the saturation of the two dimensional torque in which we adopt the horseshoe width at low softening length (i.e. low altitude). While this may be marginally true for the vortensity related corotation torque and more generally for all the bulk terms, it is likely a correct procedure for the entropy related torque and more generally all the edge terms, the contribution of which is thought to arise mainly from the equatorial regions (Masset & Casoli 2009). We therefore adopt for

the horseshoe width the simple value

$$x_s = \frac{3}{2}a\sqrt{\frac{q}{h}}, \quad (157)$$

which is close to the maximal value found by Paardekooper & Papaloizou (2009b). We stress that this approximate value is required only to estimate the arguments of the saturation functions, not the torque magnitude itself. The uncertainty on these arguments due to the uncertainty on the value of  $x_s$  is much less than the uncertainty arising from our ignorance of diffusive processes in protoplanetary disks.

### 7.3. A note on the cut-off functions

Accounting for the behaviour of the entropy related corotation torque at large diffusion requires to take into account the decay of the torque towards its linear value (Paardekooper & Papaloizou 2009a), using the cutoff functions evaluated in section 5.4.1. We note however, as mentioned above, that we do not expect the same value in the limit of a large viscosity (where we should recover the linear estimate) and in the limit of a large diffusivity (where we should get rid of the entropy related torque, as the fluid becomes isothermal). For the sake of simplicity we make the conservative assumption that the torque limit vanishes in both cases, motivated by the fact that the horseshoe drag edge term should be significantly larger than the entropy related linear corotation torque (Paardekooper & Papaloizou 2008).

Regarding the cutoff of the bulk term, we use a linear vortensity related torque value that is 2/3 of the corresponding horseshoe drag, by comparing the value given by Masset & Casoli (2009) in Eq. (102) to that given by Tanaka et al. (2002). We note that there is no need to apply a cut-off at large thermal diffusion to the bulk term arising from the entropy-vortensity viscous coupling, as this term is negligible in the limit of large thermal diffusion.

## 8. GENERALIZED TORQUE EXPRESSION

In this section we provide the torque formulae that apply to low mass planets embedded in viscous disks with thermal diffusion. For the convenience of the reader mainly interested in the results rather than in the derivation, this section is self-contained.

All the torque values given below are expressed in terms of the canonical torque value  $\Gamma_{\text{ref}}$  given by:

$$\Gamma_{\text{ref}} = \Sigma_c \Omega_p^2 a^4 q^2 h^{-2}, \quad (158)$$

where the reader is referred to Tab. 1 for the notation. The total tidal torque  $\Gamma_{\text{tot}}$  exerted by the disk on the planet features two components: the differential Lindblad torque  $\Gamma_{\text{LR}}$  and the (non-linear) corotation torque or horseshoe drag  $\Gamma_{\text{CR}}$ :

$$\Gamma_{\text{tot}} = \Gamma_{\text{LR}} + \Gamma_{\text{CR}}. \quad (159)$$

The differential Lindblad torque is given by Tanaka et al. (2002):

$$\frac{\Gamma_{\text{LR}}}{\Gamma_{\text{ref}}} = -(2.3 + 0.4\beta - 0.1\alpha)f\left(\frac{\kappa}{\kappa_c}, \gamma\right), \quad (160)$$

where  $\kappa_c$  is defined by Eq. (154) and the function  $f$  is defined by Eq. (156). We note that there has been

some recent controversy on the coefficient of the temperature gradient  $\beta$ . Paardekooper et al. (2009) give in their Eq. (14) a coefficient as large as 1.7, which is corroborated by two dimensional numerical simulations with a fixed smoothing length of the potential. We quote here the coefficient 0.4 derived from the data provided by Tanaka et al. (2002). A definite answer to this issue awaits dedicated three dimensional calculations, such as those of D'Angelo et al. (2003), with a systematic exploration of the temperature gradient. Such calculations are under way, and seem to indicate that the expression of Tanaka et al. (2002) is correct, with a high accuracy (D'Angelo, priv. comm.).

The multiplication by the function  $f$  in Eq. (160) is intended to account for the mild dependence of the Lindblad torque on the diffusivity. When the latter is small enough (namely, when the relaxation timescale of temperature disturbances is larger than the dynamical time), one may substitute the function  $f$  by the constant  $1/\gamma$ .

The horseshoe drag features, in general, two terms: a bulk term  $\Gamma_{\text{HS}}$  and an edge term  $\Gamma_{\partial\text{HS}}$ :

$$\Gamma_{\text{CR}} = \Gamma_{\text{HS}} + \Gamma_{\partial\text{HS}}. \quad (161)$$

The bulk term, using Eq. (129) and applying the normalization provided by Eq. (101) of Masset & Casoli (2009), is given by:

$$\frac{\Gamma_{\text{HS}}}{\Gamma_{\text{ref}}} = 7.8z_{\nu} \left[ \mathcal{V}F(z_{\nu}) - 2\mathcal{S} \left( \frac{z_{\nu}F(z_{\nu}) - z_{\kappa}F(z_{\kappa})}{z_{\nu} - z_{\kappa}} \right) \right] + 0.62\mathcal{V}(1 - \varepsilon_b), \quad (162)$$

where  $z_{\nu}$  and  $z_{\kappa}$  are defined respectively at Eqs. (79) and (81), and where the function  $F$  is defined by Eq. (120). The value of  $x_s$ , the half width of the horseshoe region, that is needed for the estimate of  $z_{\nu}$  and  $z_{\kappa}$ , is given by Eq. (157). Finally, Eq. (162) also displays the bulk cutoff function  $\varepsilon_b$ , given by Eq. (70), and which can be recast, using Eq. (64) of Baruteau & Masset (2008), as:

$$\varepsilon_b \sim (1 + 30hz_{\nu})^{-1}. \quad (163)$$

The edge horseshoe drag, using Eqs. (150), (151), (153) and applying the normalization provided by Eq. (98) of Masset & Casoli (2009), is given by:

$$\frac{\Gamma_{\partial\text{HS}}}{\Gamma_{\text{ref}}} = -3.3\mathcal{S} \overline{1.4z_{\kappa}^{1/2}} \overline{\varepsilon_{\kappa} 1.8z_{\nu}^{1/2}} \varepsilon_{\nu}, \quad (164)$$

where, using respectively Eqs. (71) and (72):

$$\varepsilon_{\nu} \sim [1 + (6hz_{\nu})^2]^{-1} \quad (165)$$

$$\varepsilon_{\kappa} \sim (1 + 15hz_{\kappa})^{-1} \quad (166)$$

and where

$$\overline{X} \equiv \min(1, X). \quad (167)$$

The set of Eqs. (159) to (167) provides self-contained torque formulae for a low mass planet in a disk with arbitrary viscosity and thermal diffusivity. In the particular case in which viscosity and thermal diffusivity remain moderate (more precisely when  $z_{\nu, \kappa} \ll h^{-1}$ ), one may drop the cutoff coefficients  $\varepsilon_{b, \nu, \kappa}$ , which are then close to unity.

We comment that the estimate of the bulk term of the horseshoe drag, given by Eq. (162), is more accurate and robust than the estimate of the horseshoe edge

term, given by Eq. (164), which heavily depends on small scale properties of the flow in the vicinity of the stagnation point of the horseshoe region, as was shown by Masset & Casoli (2009) and as was emphasized in section 6.5.1. Also, the factor 3.3 that features in this equation, which stems from the conservative estimate of Masset & Casoli (2009), is a minimum value. In any case, this factor is large and should be sufficient to halt migration at locations where the entropy gradient is negative and sufficiently large in absolute value, and where the viscosity and thermal diffusivity have adequate values to prevent saturation. As a consequence, a minor change in the value of this coefficient should have little qualitative impact on scenarios of migration.

## 9. DISCUSSION

### 9.1. On the planetary mass range relevant to this analysis

The torque expressions provided here are strictly valid in the regime of small planetary mass, for which the torque scales as the square of the planet mass (and the horseshoe width scales as the square root of the planetary mass). Masset et al. (2006) have shown, by means of a two dimensional analysis, that when the planetary Hill radius represents some fraction of the disk pressure length scale (typically such that  $q/h^3 \sim 0.6$  in their study), the horseshoe zone width is much larger than predicted by the  $q^{1/2}$  scaling, extrapolated from lower masses, thereby boosting the corotation torque. Paardekooper & Papaloizou (2009b) have shown that this behavior is due to the wake, which, owing to its proximity, affects the enthalpy at the horseshoe stagnation point, hence it affects the horseshoe width. They found this behavior to be smoothing dependent: the mass at which the horseshoe drag boost is observed depends on the softening length, and is smaller at smaller softening length. If one translates this in terms of altitude in a three dimensional disk, this suggests that the horseshoe region is always over wide in the vicinity of the equator, over a vertical length scale that increases when the planetary mass does. The vertically integrated bulk horseshoe drag should then be boosted when the vertical extent of the over wide region represents a significant fraction of the disk thickness. This expectation yields a relationship similar to that quoted above, i.e. one expects the boost to occur for  $q/h^3 \sim O(1)$ , where the dimensionless number of the right hand side is still to be determined by three dimensional calculations. We comment however that the edge term of the horseshoe drag, which is biased towards low altitude regions owing to its dependence in  $\varepsilon^{-1}$  (see Masset & Casoli 2009) should be boosted at planetary masses even lower than the bulk term. This constitutes another reason why the edge horseshoe drag given by Eq. (164) should be regarded as a conservative estimate, even for planetary masses significantly smaller than  $0.6h^3M_*$ .

### 9.2. Relevance of a diffusion equation to model the entropy evolution

We have modelled the radiative processes at work in the disk by a simple radial diffusion equation on the entropy. The merits of this simple approach have been discussed in section 2.5. The actual processes that con-



tribute to the energy balance of fluid elements in the disk, however, cannot be reduced to this simple minded approach. Kley & Crida (2008) have for instance performed numerical simulations that take into account, in addition to the processes that can be described as a diffusion, the local processes that affect the energy balance, i.e. the viscous heating and the radiative losses through the disk photospheres. If one neglects the diffusion and takes into account only local processes, then an alternate simple model of thermal processes can be achieved by imposing a local temperature prescription, together with a characteristic decay time of the temperature disturbances (e.g. Baruteau 2008). What matters in assessing the magnitude of the entropy-related horseshoe drag is the value of the entropy at the separatrices upstream of the U-turns. The latter results, in steady state, from a balance between libration and relaxation. We note that the dimensionless variable  $z_\kappa$ , which is used to quantify the corotation torque saturation due to thermal processes, scales with the ratio of the libration time to the thermal timescale  $\tau_{\text{th}} = x_s^2/\kappa$ :

$$z_\kappa = \frac{3}{4\pi} \frac{\tau_0}{\tau_{\text{th}}}. \quad (168)$$

Although we have not undertaken a systematic exploration of the torque saturation in the framework of a temperature prescription such as the one of Baruteau (2008), we note that his results are compatible with the formulae of Eq. (164) in which one adopts the value of  $z_\kappa$  given by Eq. (168). In a more general manner, we suggest that Eq. (168) be systematically used to assess the degree of saturation of the entropy-related corotation torque, and that  $\tau_{\text{th}}$ , the relaxation timescale of temperature disturbances of scale length  $x_s$ , be determined by a prior analysis of the relevant thermal processes.

### 9.3. Planet-disk relative drift

In the calculations performed for the analysis of the entropy related horseshoe drag, we have imposed a power law for the kinematic viscosity that yields no radial drift in the unperturbed disk. We do not expect that a relative drift of the disk and planet, given either by the large scale accretion of the disk's material onto the primary, or migration, or an admixture of both processes, would alter our conclusions, for the following reasons:

- The planet-disk drift turns out to be unimportant in the barotropic case. By extension, it should be of little importance for the bulk term of the horseshoe drag in the general case.
- The viscous drift of the vortensity sheets at the separatrices, over a synodic period, typically amounts to  $\tau_0\nu/a$ , whereas its viscous spread reads  $\sqrt{4\nu\tau_0}$ . The ratio of these two quantities is  $\nu\Omega_p^{-1}/ax_s$ , which should be small in any realistic disk and for any low mass planet for which planetary migration is relevant.
- We can also work out the typical amount of drift due to type I migration, at a typical speed  $\dot{a}$  given by

$$\dot{a} \sim \frac{2\Gamma_{\text{ref}}}{\Omega_p M_p a} \quad (169)$$

The drift induced by migration over a synodic period  $\tau_0\dot{a}$  is therefore:

$$\tau_0\dot{a} \sim \frac{8}{3} \frac{\mu_d}{h} x_s, \quad (170)$$

where  $\mu_d = \pi\Sigma_0 a^2/M_*$  is the reduced disk mass. Eq. (170) shows that the drift is a small fraction of  $x_s$  except in very massive disks, close to their gravitational stability limit. Since the drift is a tiny fraction of the horseshoe zone width, it may impact the degree of saturation only in the cases for which the viscous spread of the vortensity sheets is also a tiny fraction of the horseshoe width, that is to say when the entropy related torque is significantly saturated.

## 10. SUMMARY

We have undertaken a study of the corotation torque saturation, as a function of viscosity and thermal diffusion, and we have obtained asymptotic torque expressions that are given in section 8. A property that is essential to our derivation is that the horseshoe drag, whether barotropic or not, depends exclusively on the distribution of vortensity within the horseshoe region, so that our analysis essentially reduces to finding the vortensity distribution for a steady flow in the corotating frame. In particular, the contribution of the under- or over-dense regions that appear within the horseshoe region should not be added “manually” to the horseshoe drag estimate. Doing so leads to a violation of first principles, as is discussed in section 6.5.1. Our analysis shows that the saturated horseshoe drag can be decomposed into a bulk term and an edge term. The latter scales with the entropy gradient, as in an unsaturated situation, and its saturation properties depend both on the viscosity and on the thermal diffusivity. The bulk term, however, not only depends on the vortensity gradient, as in the unsaturated case, but also on the entropy gradient, as a result of the viscous production of vortensity at steep entropy gradients.

We have also contemplated in section 7.1 the transition from the isothermal to adiabatic differential Lindblad torque (the latter is a factor  $\gamma$  than the former), and found that it occurs when the thermal timescale is of the order of the dynamical timescale. The dependence of the entropy related torque on the thermal timescale is regulated by a markedly different ratio, namely the ratio of the thermal timescale to the libration timescale, which gives the degree of saturation.

At large viscosity or thermal diffusivity, the horseshoe drag is found to decay. We have made an attempt to account for this decay by the use of *ad hoc* simple analytical fits (cutoff functions). A detailed study of the intermediate regime that settles at large diffusion (be it viscous or thermal), and that yields a torque value comprised between the horseshoe drag and the linear corotation torque could be useful for sub-terrestrial mass objects embedded in disks with significant viscosity or short radiative timescales. One can estimate the value required for the viscosity or thermal diffusion to recover the linear regime. Writing that  $\varepsilon_{b,\nu,\kappa} \ll 1$ , we are left with, using Eqs. (163), (165) and (166):

$$\frac{\nu \text{ or } \kappa}{a^2\Omega} \gg 0.1q^{3/2}h^{-5/2}. \quad (171)$$

For the condition on viscosity, this can be translated into a lower limit on the  $\alpha$  coefficient of the disk:

$$\alpha \gg 0.1q^{3/2}h^{-9/2}. \quad (172)$$

Eqs. (171) and (172) show that the corotation torque should approach its linear value for an Earth mass planet in a disk with  $h = 0.04$ , invaded by magnetorotational turbulence (the critical  $\alpha$  value of the right hand side of Eq. (172) being then  $10^{-3}$ ). If the planet has a higher mass, if the disk is thinner, or if the planet is in the dead zone, the corotation torque should be determined by a horseshoe drag analysis.

Finally, we have underlined that the horseshoe drag edge term is potentially extremely strong in a three dimensional case, so that the estimate that we have given in Eq. (164) should be regarded as conservative. This stresses the need for a three dimensional study, that would allow a calibration of the unsaturated edge term value.

The numerical simulations performed in this work have been run on a 140 core cluster funded by the program *Origine des Planètes et de la Vie* of the French *Institut National des Sciences de l'Univers*. Partial support from the COAST project (*COmputational ASTrophysics*) of the CEA is also acknowledged. F.M. also wishes to thank G. Koenigsberger for hospitality at the *Instituto de Ciencias Físicas* of UNAM, Mexico.

#### REFERENCES

- Alibert, Y., Mordasini, C., Benz, W., & Winisdoerffer, C. 2005, *A&A*, 434, 343
- Balbus, S. A., & Hawley, J. F. 1991, *ApJ*, 376, 214
- Baruteau, C. 2008, PhD thesis, Ecole Doctorale d'Astronomie et d'Astrophysique d'Ile de France, Observatoire de Paris, F-75014, Paris, France
- Baruteau, C., & Lin, D. N. C. 2010, *ApJ*, 709, 759
- Baruteau, C., & Masset, F. 2008, *ApJ*, 672, 1054
- Casoli, J., & Masset, F. S. 2009, *ApJ*, 703, 845
- D'Angelo, G., Kley, W., & Henning, T. 2003, *ApJ*, 586, 540
- Fromang, S., Papaloizou, J., Lesur, G., & Heinemann, T. 2010, in *EAS Publications Series*, Vol. 41, *EAS Publications Series*, ed. T. Montmerle, D. Ehrenreich, & A.-M. Lagrange, 167–170
- Ida, S., & Lin, D. N. C. 2004a, *The Astrophysical Journal*, 604, 388
- . 2004b, *The Astrophysical Journal*, 616
- . 2005, *The Astrophysical Journal*, 626, 1045
- . 2008a, *The Astrophysical Journal*, 673, 487
- . 2008b, *The Astrophysical Journal*, 685, 584
- Johnson, E. T., Goodman, J., & Menou, K. 2006, *ApJ*, 647, 1413
- Kley, W. 1998, *A&A*, 338, L37
- Kley, W., & Crida, A. 2008, *A&A*, 487, L9
- Masset, F. 2000a, *A&AS*, 141, 165
- Masset, F. S. 2000b, in *Astronomical Society of the Pacific Conference Series*, Vol. 219, *Disks, Planetesimals, and Planets*, ed. G. Garzón, C. Eiroa, D. de Winter, & T. J. Mahoney, 75–+
- Masset, F. S. 2001, *ApJ*, 558, 453
- Masset, F. S. 2008a, in *EAS Publications Series*, Vol. 29, *EAS Publications Series*, ed. M.-J. Goupil & J.-P. Zahn, 165–244
- Masset, F. S. 2008b, in *IAU Symposium*, Vol. 249, *IAU Symposium*, ed. Y.-S. Sun, S. Ferraz-Mello, & J.-L. Zhou, 331–346
- Masset, F. S., & Casoli, J. 2009, *ApJ*, 703, 857
- Masset, F. S., D'Angelo, G., & Kley, W. 2006, *ApJ*, 652, 730
- Masset, F. S., & Papaloizou, J. C. B. 2003, *ApJ*, 588, 494
- Meyer-Vernet, N., & Sicardy, B. 1987, *Icarus*, 69, 157
- Mordasini, C., Alibert, Y., & Benz, W. 2009a, *A&A*, 501, 1139
- Mordasini, C., Alibert, Y., Benz, W., & Naef, D. 2009b, *A&A*, 501, 1161
- Nelson, R. P. 2005, *A&A*, 443, 1067
- Paardekooper, S., Baruteau, C., Crida, A., & Kley, W. 2009, *ArXiv e-prints*
- Paardekooper, S.-J., & Mellema, G. 2006, *A&A*, 459, L17
- Paardekooper, S.-J., & Papaloizou, J. C. B. 2008, *A&A*, 485, 877
- . 2009a, *MNRAS*, 394, 2283
- . 2009b, *MNRAS*, 394, 2297
- Stone, J. M., & Norman, M. L. 1992, *ApJS*, 80, 753
- Tanaka, H., Takeuchi, T., & Ward, W. R. 2002, *ApJ*, 565, 1257
- Thommes, E. W., Matsumura, S., & Rasio, F. A. 2008, *Science*, 321, 814
- Thommes, E. W., & Murray, N. 2006, *ApJ*, 644, 1214
- Thommes, E. W., Nilsson, L., & Murray, N. 2007, *ApJ*, 656, L25
- van Leer, B. 1977, *Journal of Computational Physics*, 23, 276
- Ward, W. R. 1991, in *Lunar and Planetary Institute Conference Abstracts*, 1463–+
- Ward, W. R. 1997, *Icarus*, 126, 261
- Ward, W. R. 2007, in *Lunar and Planetary Institute Science Conference Abstracts*, Vol. 38, *Lunar and Planetary Institute Science Conference Abstracts*, 2289–+